

Initial PET Performance Evaluation of a Preclinical Insert for PET/MRI with Digital SiPM Technology

David Schug¹, Christoph Lerche^{2,3}, Bjoern Weissler^{1,4},
 Pierre Gebhardt⁵, Benjamin Goldschmidt¹, Jakob Wehner¹,
 Peter Michael Dueppenbecker^{4,5}, Andre Salomon²,
 Patrick Hallen¹, Fabian Kiessling⁶, and Volkmar Schulz^{1,4}

¹Physics of Molecular Imaging Systems, Experimental Molecular Imaging,
 RWTH Aachen University, Aachen, Germany

²Oncology Solutions, Philips Research, Eindhoven, Netherlands

³Institute of Neuroscience and Medicine (INM-4), Forschungszentrum Jülich
 GmbH, Jülich, Germany

⁴Clinical Application Research, Philips Research, Aachen, Germany

⁵Imaging Sciences and Biomedical Engineering, King's College London, London,
 United Kingdom

⁶Experimental Molecular Imaging, RWTH Aachen University, Aachen, Germany

E-mail: schug@pmi.rwth-aachen.de and schulz@pmi.rwth-aachen.de

Abstract. Hyperion-II^D is a positron emission tomography (PET) insert which allows simultaneous operation in a clinical magnetic resonance imaging (MRI) scanner. To read out the scintillation light of the employed LYSO crystal arrays with a pitch of 1 mm and 12 mm in height, digital silicon photomultipliers (*DPC 3200-22*, Philips Digital Photon Counting) (DPC) are used. The basic PET performance in terms of energy resolution, coincidence resolution time (CRT) and sensitivity as a function of operating parameters, such as the operating temperature, the applied overvoltage, activity and configuration parameters of the DPCs, were evaluated on system level. The measured energy resolution did not show a large dependency on the selected parameters and is in the range of 12.4%–12.9% for low activities and degrades to ~13.6% at activities of ~100 MBq. The CRT strongly depends on the selected trigger scheme (trig) of the DPCs. We measured approximately 260 ps, 440 ps, 550 ps and 1300 ps for trig 1-4, respectively. The true sensitivity for a NEMA NU 4 mouse-sized scatter phantom with a 70-mm-long tube of activity was dependent on the operating parameters and was determined to be 0.4%–1.4% at low activities. The random fraction stayed below 5% at activities up to 100 MBq and the scatter fraction was evaluated as ~6% for an energy window of 411 keV–561 keV and ~16% for 250 keV–625 keV. Furthermore, we performed imaging experiments using a mouse-sized hot-rod phantom and a large rabbit-sized phantom. In 2D slices of the reconstructed mouse-sized hot-rod phantom ($\mathcal{O} = 28$ mm), the rods were distinguishable from each other down to a rod size of 0.8 mm. There was no benefit of the better CRT of trig 1 over trig 3, where in the larger rabbit-sized phantom ($\mathcal{O} = 114$ mm), we could show a clear improvement of image quality using the time-of-flight information. The findings will allow system architects, aiming at a similar detector design using DPCs, to make predictions about the design requirements and the performance that can be expected.

Keywords: PET, preclinical, time-of-flight, digital SiPM, DPC

Submitted to: *Phys. Med. Biol.*

1. Introduction

Positron emission tomography (PET) is a very sensitive functional imaging modality, e.g. for metabolic processes, but it provides almost no anatomical information. To allow anatomical co-registration, PET was successfully integrated with X-ray computed tomography (CT). However, PET/CT exposes the patients to an additional radiation dose, offers only limited soft tissues contrast and does not allow simultaneous imaging. The combination of PET with magnetic resonance imaging (MRI) promises to overcome those shortcomings (Buchbender et al. 2012a; Buchbender et al. 2012b; Schulthess and Schlemmer 2009; Jadvar and Colletti 2014; Drzezga et al. 2012). Designing a PET/MRI system is challenging due to the high static magnetic field, the fast switching gradient fields and the radio frequency (RF) system needed for an MR image acquisition (Vandenbergh and Marsden 2015). PET/MRI offers real simultaneous image acquisition, provided that the interference between both modalities is reduced to a tolerable level.

Until recently, conventional PET detectors were based on photomultiplier tubes which cannot be operated inside strong magnetic fields. Therefore, silicon-based photo detectors are commonly used for PET/MRI applications. An overview of designs that combine PET with MRI can be found in Pichler et al. (2008), Zaidi and Del Guerra (2011), Disselhorst et al. (2014), and Vandenbergh and Marsden (2015).

Analog silicon photomultipliers (SiPMs) are made up of an array of highly sensitive single photon avalanche diodes (SPAD) which give an analog avalanche signal for each breakdown. All SPADs are coupled together and the sum of the current signal is proportional to the number of SPADs that break down. The analog SiPM's signal output is influenced by voltage and temperature changes and depends on the photon detection efficiency (PDE) as well as the gain of individual SPADs.

Digital SiPMs (dSiPMs) are the latest evolutionary step in silicon-based photo detectors. They digitize and actively quench the breakdown of individual single SPADs. The digitized breakdowns are summed up digitally and can be handled using digital signal processing techniques. The number of SPAD breakdowns, the dSiPM's signal output, is mainly influenced by the change of the SPAD PDE and not by the SPAD gain, as long as the breakdown is detected (Frach et al. 2009). Furthermore, dSiPMs are good candidates to build up robust PET systems that can be operated inside an MRI environment, as no analog signal transmission lines before digitization are needed. In 2009, Philips Digital Photon Counting (PDPC) presented the first implementation of a dSiPM, the so-called digital photon counter (DPC) (Frach et al. 2009; Degenhardt et al. 2009).

So far, investigations of the DPC for PET applications were mainly conducted using small demonstrators based on the technology evaluation kit (TEK) provided by PDPC. For example, the influence of DPC configuration parameters on the read-out probability (Tabacchini et al. 2014) and on the number of counted photons (Dam et al. 2012) was investigated. The timing performance of TEK-based gamma detectors was evaluated (Dam et al. 2013). Scintillator arrangements ranging from pixelated (Yeom et al. 2013; Schug et al. 2013; Georgiou et al. 2014; Marcinkowski et al. 2014) to monolithic scintillators (Seifert et al. 2013) were implemented on the TEK. Only a few imaging-capable demonstrators using DPCs on the TEK were presented (España et al. 2014; Schneider et al. 2015). Apart from a single demonstrator built up by PDPC (Degenhardt et al. 2012) and results presented for a clinical PET/CT (Miller et al. 2014), DPCs have not been investigated on the larger system level, yet. The

presented system, developed in our group, was used to perform the first extensive performance study of a DPC-based preclinical PET.

We developed the first MRI-compatible PET insert, called Hyperion-II^D, on basis of DPCs installed on an MRI-compatible read-out infrastructure designed in our group (Weissler et al. 2012; Weissler et al. 2015). The predecessor, based on a similar architecture employing analog SiPMs with ASICs, Hyperion-I, is discussed in Weissler et al. (2014). For both versions of the platform, the complete digitization is performed inside the MRI and digital information is sent out via optical ethernet links to a data acquisition server. First results on the PET/MRI interferences of the Hyperion-II^D platform using DPCs were presented in Wehner et al. (2014), Schug et al. (2015a), and Weissler et al. (2015). A detailed interference study was presented in Wehner et al. (2015).

Hyperion-II^D employs sensor tiles which are specially optimized for MR compatibility, but similar in terms of the geometrical layout to the sensor tiles distributed by PDPC. The scanner houses 60 sensor tiles, while the TEK platform can be used to read out a maximum of 4 tiles with the Tile TEK and 8 tiles with the Module TEK and thus offers only a limited maximum sensitivity, bore size and limits PET performance evaluations to small system designs. In this work, we investigated the influence of the DPC operating parameters on the PET performance of the insert equipped with a preclinical scintillator configuration outside an MRI system. The used data processing and calibration techniques were presented in Schug et al. (2015b) and can be used on a wide range of system designs based on DPCs utilizing a similar scintillator geometry. We evaluated the influence of operating parameters, such as temperature and the applied voltage, as well as DPC configuration parameters on the energy resolution, the timing performance, the sensitivity and the spatial image resolution of the insert. The findings shall allow system architects, aiming at a similar detector design using DPCs, to make predictions on the design requirements and the performance that can be expected.

2. Materials

2.1. Hyperion-II^D PET insert

The Hyperion-II^D platform is described in detail in Weissler et al. (2012) and Weissler et al. (2015). In Schug et al. (2015b), we give a detailed overview of the detector components that are relevant for gamma detection.

The detector stack consists of a pixelated scintillating crystal array coupled via a light guide to a sensor tile which is used to read out the scintillation light and an FPGA-based control and read-out board (interface (IF) board) (Dueppenbecker et al. 2012b) (Figure 1a). 30×30 optically isolated, cerium-doped lutetium yttrium orthosilicate (LYSO) crystals with a size of $0.933 \times 0.933 \times 12 \text{ mm}^3$ and a pitch of 1 mm are mounted on a 2 mm thick glass light guide. The sensor tile is $32.6 \times 32.6 \text{ mm}^2$ in size and is made up of 16 DPC 3200-22 sensors from PDPC with 2×2 pixels each (Frach et al. 2009; Degenhardt et al. 2009; Frach et al. 2010; Degenhardt et al. 2010) resulting in 8×8 readout channels per sensor tile. The 3200 SPADs per DPC pixel can be deactivated individually in order to reduce the overall dark count rate (DCR) of the DPC.

A trigger scheme (trig) can be set between 1-4 resulting in $1, 2.33 \pm 0.67, 3.0 \pm 1.4$ and 8.33 ± 3.80 mean number of SPAD breakdowns per pixel in order to generate

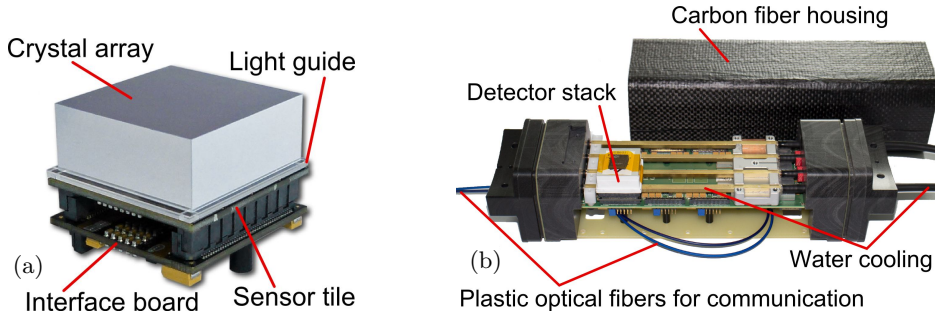


Figure 1. (a) the detector stack consists of an interface board, the sensor tile and a pixelated scintillating crystal array mounted on a light guide (© [2012] IEEE. Reprinted, with permission, from Weissler et al. (2012)). (b) the singles detection module is able to house up to six stacks. Only one detector stack is mounted to reveal the cooling pipes (reprinted from Wehner et al. (2014)).

a trigger, respectively. Setting the trig to low values results in a better timing performance, but increases the likelihood to generate a trigger on dark counts, which may result in a higher dead time and lower sensitivity. The row-trigger-line refresh feature can help to reduce the dark-noise-induced triggers and is used throughout this work (for details and explanation see Schug et al. (2015b) and Marcinkowski et al. (2013)).

When the trigger condition is met, a time stamp is generated and the DPC enters a validation phase of programmable length. The configurable validation scheme (val) determines the threshold of SPAD breakdowns which has to be reached during the validation phase. After validation, the integration phase is started, the DPC sums up the SPAD breakdowns and the hit data is transmitted. Details of the trig and val and the resulting thresholds can be found in Tabacchini et al. (2014) and Philips Digital Photon Counting (2014). The val used in this work are listed in Table 1.

The IF board houses an FPGA which is used to control voltages and to configure and read out the DPCs of the sensor tile as well as a temperature sensor located on the backside of the latter. The main voltage lines controlled by the IF board are the V_{util} and V_{bias} lines. V_{bias} sets the operating voltage of the SPADs. The SPADs should be operated at an excess voltage (overvoltage, V_{ov}) in the range of about $V_{ov} = 2\text{ V} - 3.3\text{ V}$ above the measured breakdown voltage (V_{bd}) (manufacturer default: $V_{ov} = 3\text{ V}$). V_{util} is used to actively quench and recharge SPADs. It has to be larger than V_{ov} to ensure stable quenching of SPADs and an additional safety margin of at least 0.2 V should be taken into account (Philips Digital Photon Counting 2014).

Table 1. DPC-3200-22 validation schemes in the notation used throughout the text, hexadecimal notation and in the notation used by PDPC and the resulting validation threshold per pixel (taken from Thon 2012, partly published in Philips Digital Photon Counting 2014 and Tabacchini et al. 2014).

val(text)	val(hex)	val(PDPC)	avg. SPADs	min. SPADs
17ph	0x55:0R	4-OR	16.9 ± 6.2	4
28ph	0x54:0R	n.a.	27.5 ± 10.3	4
37ph	0x50:0R	n.a.	37.1 ± 12.8	6
52ph	0x00:0R	8-OR	52.2 ± 15.0	8

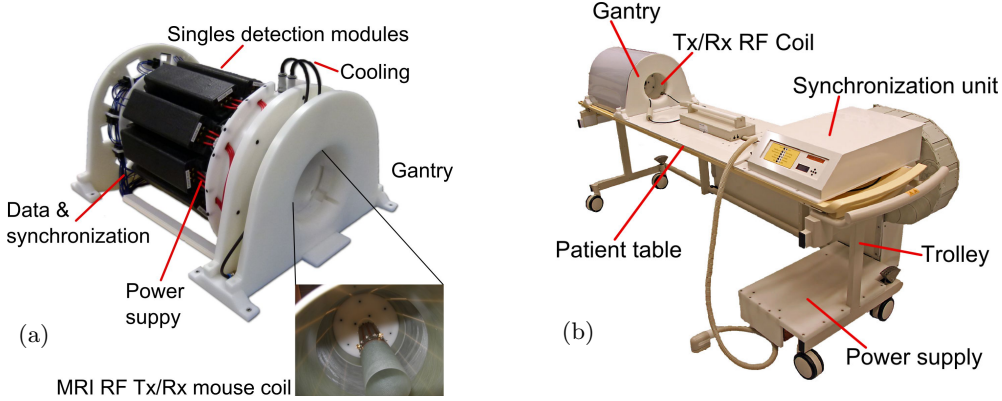


Figure 2. (a) the gantry of the PET insert holds ten SDMs (© [2012] IEEE. Reprinted, with permission, from Weissler et al. (2012)). (b) the gantry, a synchronization unit and power supply is mounted on a trolley which allows easy insertion into an MRI scanner. Only a single data link, a power cable and the cooling tubes have to be connected.

The employed low-dropout regulator for V_{util} introduces a 100 mA current limitation on the I_{util} line. Especially trig 1 causes a high load on the I_{util} line due to many dark noise induced triggers, especially at high temperatures, and may be influenced by the current limitation.

2×3 detector stacks with a pitch of 33.3 mm (Figure 1b) are mounted on a singles detection module (SDM). SDMs are equipped with an optical gigabit Ethernet (GbE) interface. They are cooled using a liquid cooling system with a process thermostat (Lauda Integral XT 150, Germany) and are flooded with dry air. The liquid cooling pipes run between the IF board and the sensor tile. The SDMs are shielded with a light- and RF-tight housing made from a 0.8-mm-thick carbon fiber composite (Dueppenbecker et al. 2012a).

The insert is composed of ten SDMs mounted on a gantry and a synchronization unit distributes a reference clock and trigger signals. They make build a PET system with an inner diameter (distance of opposing inner crystal surfaces) of 209.6 mm and an axial field of view (FOV) of 97 mm (Figure 2a). The gantry is able to house radio-frequency transmit and receive (RF Tx/Rx) coils with a maximized gamma transparency and different inner bore sizes (Weissler et al. 2015) which are only installed as a passive component in this study. We mainly used a small RF Tx/Rx coil with an inner diameter of 46 mm. To measure a rabbit-sized phantom, we installed a larger RF Tx/Rx coil with an inner diameter of 160 mm.

The insert, the synchronization unit and a power supply are mounted on a trolley which allows easy installation in a Philips Achieva MRI system (Figure 2b). All SDMs are linked via the GbE interfaces to a Data Acquisition and Processing Server (DAPS) which is connected to a control computer running a monitoring and controlling software (Gebhardt et al. 2012). The DAPS can be used to store the raw DPC sensor data for offline analysis or it can process the DPC data to coincident listmode data in real time (Goldschmidt et al. 2013). Control and status data are routed from the control PC to the system and vice versa.

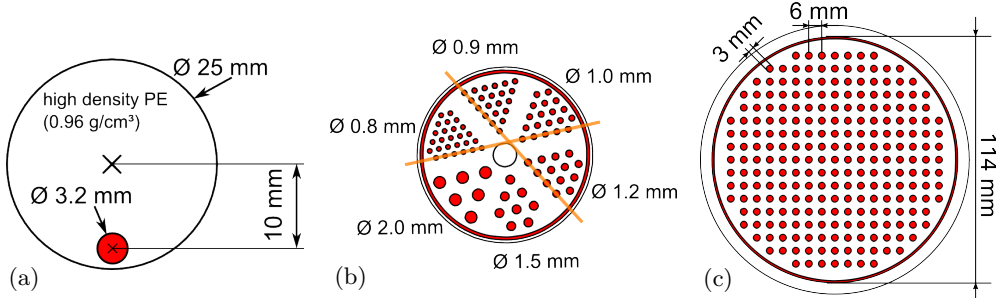


Figure 3. (a) slice through the mouse-sized scatter phantom. The scatter phantom has an axial extent of 70 mm. (b) hot-rod phantom used to investigate the spatial resolution. The structured region has an diameter of 28 mm. The evaluated profiles are marked in orange. (c) rabbit-sized phantom used to investigate the benefit of TOF information for image reconstruction. The structured part of the phantoms (b) and (c), for which the slices are shown, have an axial extent of 20 mm. The FDG-filled areas are marked in red.

2.2. Testsources and Phantoms

Five point-like ^{22}Na sources with an active diameter of 0.25 mm and an activity of 1.1 MBq–1.5 MBq enclosed in a cast acrylic cube with an edge length of 10 mm (NEMA cubes) were used for performance studies under a large variety of different operating parameters at a constant activity.

A mouse-sized scatter phantom (NEMA NU 4 standard) was used for investigations of activity-dependent performance parameters including the count rate performance of the scanner (Figure 3a). The phantom has an axial extent of 70 mm and a diameter of 25 mm with a hole to hold a tube with a radioactive tracer solution. The hole is placed 10 mm off center and is 3.2 mm in diameter. The tube fits the hole and has a wall thickness of 0.5 mm. The activity was distributed over the full 70 mm of the phantom opposed to the distribution defined in the NEMA NU 4 standard (60 mm).

For image-spatial-resolution studies, we used a mouse-sized hot-rod phantom with six regions with rods of 0.8 mm, 0.9 mm, 1.0 mm, 1.2 mm, 1.5 mm and 2.0 mm in diameter, a center-to-center spacing of two times the diameter and an axial extent of 20 mm (Figure 3b).

To investigate the benefits of time-of-flight (TOF) image reconstruction, we used a rabbit-sized phantom with a diameter of 114 mm (Figure 3c). The phantom is structured with rods with a diameter of 3 mm and an axial extent of 20 mm distributed on a Cartesian grid with a pitch of 6 mm.

All phantoms were filled with a $[^{18}\text{F}]\text{Fluorodeoxyglucose}$ (FDG) solution.

3. Methods

In this work, we used the unprocessed raw DPC sensor data. An offline analysis was performed using a calibration and processing framework which is described in detail in Schug et al. (2015b). We employed a center-of-gravity (COG) method which defines a region of interest (ROI) around the pixel capturing most of the scintillation light (main pixel) of a single. The ROI includes the main pixel and the neighboring pixels. The COG with automatic corner extrapolation (COG-ACE) was used throughout

this work. It correctly handles up to two sets of DPC channels per crystal, allowing a single corner pixel to be missing and yields a superior sensitivity compared to the COG method which requires all neighboring channels (COG-FN). DPC raw photon values were corrected for saturation (Schug et al. 2015b). A correction of time stamps as a function of the light output of the scintillator (walk correction) was not applied.

3.1. Temperature Measurements

The cooling temperature T_C was set and controlled by the process thermostat. The operating temperature T_{op} was measured with the temperature sensor on the backside of the sensor tiles. A system T_{op} is reported as the mean and standard deviation of all sensor tile T_{op} readings.

3.2. Measurement of the Breakdown Voltage and Bias Voltage Regulation

By connecting the SPADs to ground and measuring the current-voltage characteristic, V_{bd} was determined for each sensor tile individually. This measurement was performed for different T_C resulting in $T_{op} \approx 0^\circ\text{C} - 27^\circ\text{C}$. To determine the dependence of the DPC's V_{bd} on T_{op} a linear regression on the measured data was performed.

For the following experiments, V_{bias} was set to a constant value prior to and not dynamically adjusted during a measurement. For one set of measurements with different T_C , V_{bias} was kept constant using the V_{bd} value obtained at $T_C = 15^\circ\text{C}$, which means that a change in T_C lead to an effective change of V_{ov} . For the other set of measurements, V_{bias} was adjusted before the start of a measurement for the selected T_C , meaning that the effective V_{ov} was kept constant as a function of T_C .

3.3. Basic PET Performance Measurements

We investigated the influence of the V_{ov} , T_C , trig, val, activity and energy window on the basic PET performance parameters: energy resolution ($\Delta E/E$), coincidence resolution time (CRT) and sensitivity. It is not feasible to scan all parameter combinations of the multi-dimensional space. Therefore, we constructed several testing scenarios around conservatively chosen benchmark points and varied parameters along some axes of the parameter space. For all measurements we inhibited 20% of the noisiest SPADs per pixel, used a validation length of 40 ns, an integration length of 165 ns and a fixed cluster window of 40 ns. We used two different energy windows: the narrow energy window (NE) ranges from 411 keV–561 keV to reject scattered gammas and discard high-light-output and pile-up events. The wide energy window (WE) was set to 250 keV–625 keV to increase the sensitivity compared to the NE. Singles were filtered before performing a coincidence search with a sliding coincidence window (CW). If not mentioned otherwise, we used CW = 400 ps, 550 ps, 650 ps and 1500 ps for trig 1-4, respectively, which corresponds to approximately $\pm 3\sigma$ CRT.

Coincidences with more than two singles were discarded. A minimal distance of 4 detector stacks between the two singles in tangential direction was required. For the rabbit-sized phantom, this was reduced to 3 detector stacks to increase the FOV.

3.3.1. ^{22}Na Point Sources: The five NEMA cubes were distributed in the FOV along the z -axis (axial). The positions and activities of the point sources are listed in Table 2. This allows a very precise determination of the CRT as each line of response (LOR) can be unambiguously assigned to one of the point sources.

For the measurement series with constant V_{bias} , we chose $V_{\text{ov}} = 2.5 \text{ V}$, $T_{\text{C}} = 15 \text{ }^{\circ}\text{C}$, trig 2 and val 17ph as our default benchmark point. Starting from this benchmark point, we investigated $V_{\text{ov}} = 2.5 \text{ V}$, 2.8 V, 2.9 V and 3.0 V and $T_{\text{C}} = -5 \text{ }^{\circ}\text{C}$, 5 $^{\circ}\text{C}$, 15 $^{\circ}\text{C}$ and 20 $^{\circ}\text{C}$, trig 1-4 and val 17ph, 28ph and 52ph. Additionally, we measured at $T_{\text{C}} = -5 \text{ }^{\circ}\text{C}$ $V_{\text{ov}} = 2.5 \text{ V}$, 2.8 V and 2.9 V. We used the NE and WE to process the data. All performed measurements and their settings are listed in supplementary Table S1.

The benchmark point for the measurement with constant $V_{\text{ov}} = 2.5 \text{ V}$ was chosen as val 17ph. We investigated $T_{\text{C}} = -5 \text{ }^{\circ}\text{C}$, 5 $^{\circ}\text{C}$, 10 $^{\circ}\text{C}$, 15 $^{\circ}\text{C}$ and 20 $^{\circ}\text{C}$ for trig 1, 3 and 4. Trig 2 was omitted as it yields similar results to trig 3, as learned from the first measurement series. All measurements and their settings are listed in supplementary Table S2.

3.3.2. FDG Mouse-Sized Scatter Phantom: We used the mouse-sized scatter phantom filled with FDG (Figure 3a) and started to measure at an activity of $\sim 110 \text{ MBq}$ down to $\sim 0.5 \text{ kBq}$. We used $T_{\text{C}} = 0 \text{ }^{\circ}\text{C}$, $V_{\text{ov}} = 2.5 \text{ V}$ and programmed the DPCs with combinations of trig 1, 2 and 3 and val 17ph, 28ph, 37ph and 52ph during the decay of the FDG. All measurements and their settings are listed in supplementary Table S3.

3.3.3. Result Extraction and Computation $\Delta E/E$ was determined using the energy spectrum of coincident singles. A Gaussian was iteratively fitted to match a fit range of -0.5 FWHM to 1.0 FWHM from the mean. No background removal or modeling was performed (see result plot Figure 4).

To show the energy spectrum of the scanner over a larger range we applied for one exemplary measurement of the mouse-sized scatter phantom only a very small lower threshold of only 100 measured photons on the channels used for energy calculation on coincident singles (Schug et al. 2015b).

The CRT was calculated by evaluating the FWHM of the spectrum of the measured timing differences between coincident singles corrected for known source positions either of the point sources or the line source. A Gaussian was iteratively fitted to match a fit range of -0.5 FWHM to 0.5 FWHM from the mean. No background removal or modeling was performed.

For measurements using the ^{22}Na point sources, the sensitivity was evaluated using the prompts rate without correcting for randoms and scatter. The branching ratio of the ^{22}Na β^+ decay of 0.906 was accounted for. The sensitivity as a function of activity was measured with the mouse-sized scatter phantom corrected for scatter and randoms. The randoms rate was estimated based on the singles rate per crystal and

Table 2. Source positions for the measurements with the five NEMA cubes.

NEMA cube	constant V_{bias}				constant V_{ov}			
	x/mm	y/mm	z/mm	activity/MBq	x/mm	y/mm	z/mm	activity/MBq
1	-0.6	-1.8	-0.5	1.48	-2.7	-11.8	-37.9	1.35
2	-1.3	-1.7	30.2	1.37	-1.9	-9.8	-18.7	1.26
3	-0.6	-1.8	-15.5	1.28	-1.6	-9.9	-1.4	1.17
4	-1.5	-1.7	14.4	1.25	-2.4	-10.9	12.9	1.15
5	-0.2	-1.8	-32.1	1.20	-2.3	-11.8	29.7	1.10

was corrected for prompts and pile-up (Oliver and Rafecas 2012). Scatter estimation was performed based on the NEMA NU 4 standard using a single sinogram (projection of all LORS on a single transaxial plane) for the whole scanner. The prompts rate, randoms rate, scatter rate and NECR were evaluated in the corridor defined in the NEMA NU 4 standard.

3.4. Imaging Experiments

All imaging experiments were conducted using the NE to suppress object scatter and trig 1 and trig 3 was employed. If not stated otherwise, the same parameters as for the basic PET performance measurements were used. Reconstructions were performed for the whole datasets of the two measurements and, for comparison, they were trimmed once for the same number of tracer decays and once for the same number of recorded coincidences. This allowed comparisons taking the respective sensitivity into account as well as neglecting it and using the same statistics.

Image reconstructions were performed using an ordered subset expectation maximization (OSEM) (Hudson and Larkin 1994) 3D reconstruction (Salomon et al. 2011; Salomon et al. 2012). After each subset of an iteration, a 3D Gaussian smoothing was performed. We used a self-normalization but did not correct for scatter and attenuation. The reconstructed activity distributions were linearly normalized using the same region of interest per phantom. The 3D data is projected on a transaxial plane using a defined extent in axial direction (slice thickness) in order to reduce the required measurement time to acquire enough coincidences for image reconstruction showing the resolution of the scanner. Specific parameters for the reconstructions are stated for the respective phantom measurement.

All of the above mentioned datasets were reconstructed with and without TOF information, and we calculated the absolute difference between the two reconstructions for each dataset. The absolute-difference images were multiplied with a factor of 5 in order to better visualize the difference using the same grayscale as used for the reconstructed data sets.

3.4.1. FDG Mouse-Sized Hot-Rod Phantom: For the mouse-sized hot-rod phantom (Figure 3b), the measurement parameters were chosen as $T_C = -5^\circ\text{C}$, $V_{ov} = 2.5\text{ V}$ and val 28ph. The trig 3 measurement was started with an activity of 9.0 MBq for a measurement time of 762 s. Approximately 8 min later, the phantom was measured at an activity of 7.9 MBq with trig 1 for 1160 s.

For the image reconstructions, we used a voxel pitch of 0.25 mm, 16 iterations, 32 subsets, applied a Gauss filter of 0.675 mm (FWHM) after each subset, and a slice thickness of 20 mm. We extracted two profiles through these slices: one profile going through the rods with a diameter of 0.9 mm and 1.2 mm, and a second profile through the rods with a diameter of 0.8 mm and 1.0 mm (Figure 3b). We calculated peak-to-valley values for each peak using the profiles. The peak height was divided by the mean height of the two adjacent valleys or, for the first and last peak, the height of the single adjacent valley.

3.4.2. FDG Rabbit-Sized Phantom: For the rabbit-sized phantom (Figure 3c), we used $T_C = -5^\circ\text{C}$, $V_{ov} = 2.5\text{ V}$ and val 28ph. A CW of 1.5 ns was used for both trig to account for the diameter of the activity distribution.

For the first experiment using this phantom, the axes of the cartesian grid on which the rods are located were aligned with the axes of the transversal plane of the scanner (see subsection 5.5 and Figure 13). The trig 3 measurement was started with an activity of 3.8 MBq for a measurement time of 1542 s. Approximately 14 min later, the phantom was measured at an activity of 3.0 MBq using trig 1 for 1018 s.

For a second experiment, the phantom was rotated around the axial axis by 9° with respect to the first experiment to break the alignment of the phantom axes with the scanner gaps (see discussion subsection 5.5). For the trig 3 measurement, an activity of 9.0 MBq was used and we measured for a duration of 762 s. Trig 1 was measured approximately 8 min later with an activity of 7.9 MBq for 1160 s.

For the image reconstructions, we used a voxel pitch of 1 mm, 16 iterations, 8 subsets, applied a Gauss filtering after each subset of 0.7 mm (FWHM) and used a slice thickness of 10 mm.

4. Results

The detailed results of all measurements using the point sources and the mouse-sized scatter phantom are listed in the supplement (Table S1, Table S2 and Table S3). We extracted graphs, showing the behavior of a performance parameter as a function of V_{ov} , system T_{op} and activity. The difference of T_C and the system's T_{op} was approximately 5 °C–10 °C under operation mainly depending on T_C , trig and the activity (for all measurements both values are reported in the supplement). Improvements and degradations are reported as relative changes.

4.1. Measurement of the Breakdown Voltage

The mean and standard deviation of V_{bd} for all sensor tiles was determined as 23.02 ± 0.12 V at $T_{op} = 15$ °C and its dependence on T_{op} as 17.1 ± 1.0 mV/K (supplementary Figure S1). T_{op} of one detector stack could not be read out due to a broken sensor and was omitted for the evaluation. Nonetheless, V_{bd} was saved for the applied values of T_C for this detector stack as well.

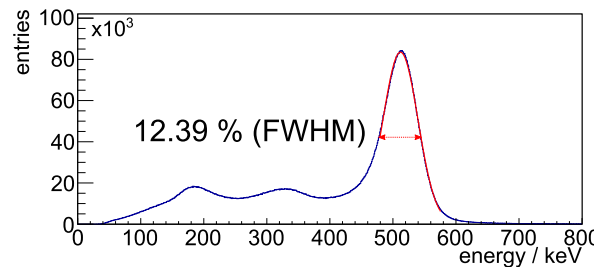


Figure 4. Exemplary and unfiltered system energy spectrum of coincident singles applying the COG-ACE algorithm requiring a minimum of 100 photons from a measurement with the FDG-filled mouse-sized scatter phantom with an activity of 8.41 MBq. The Gaussian fitted to the spectrum to evaluate the Eres, is plotted in the used fit range.

4.2. Possible Operating Parameters

Due to the current limitation on the I_{util} line, using trig 1 was limited to low temperatures and low activities. $T_C = 5^\circ\text{C}$ ($T_{\text{op}} = 13.77 \pm 1.35^\circ\text{C}$) was the highest of the tested temperatures which allowed a stable operation of trig 1 using $V_{\text{ov}} = 2.5\text{ V}$. The highest possible activity was 36.74 MBq. The other trig could be used without restrictions for all tested operation conditions.

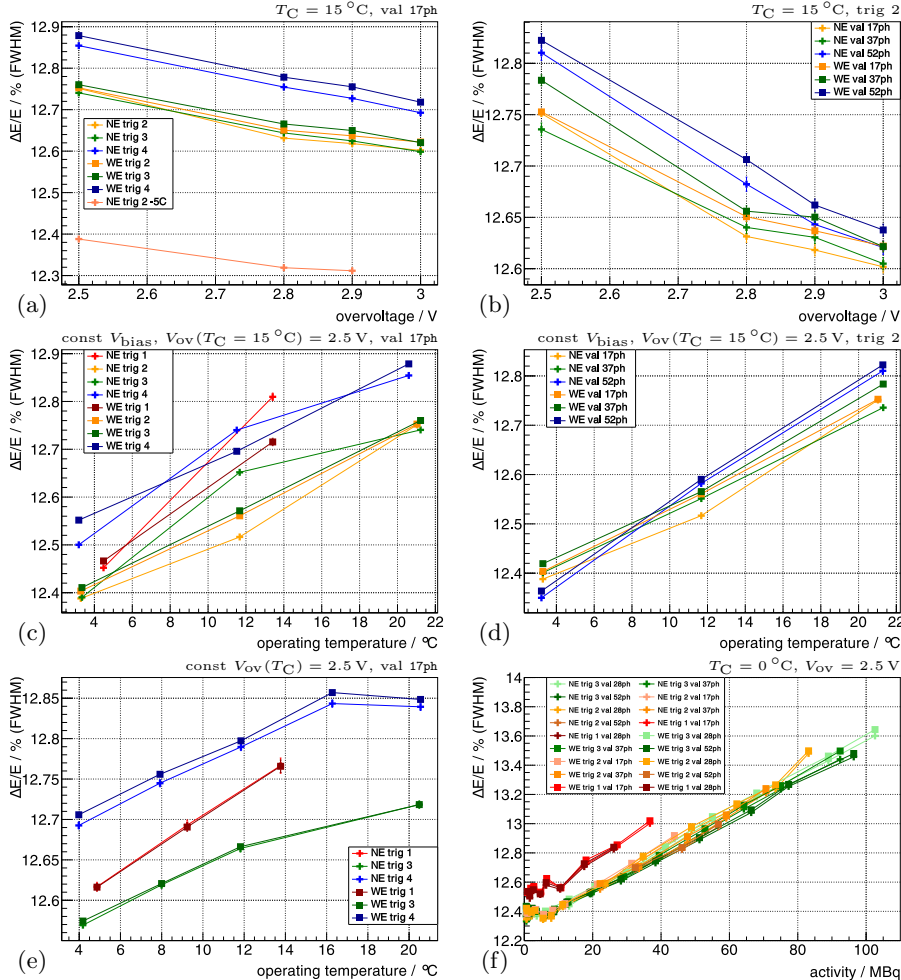


Figure 5. $\Delta E/E$ of the whole insert measured with the ^{22}Na point sources is shown as a function of V_{ov} in (a) for different trig and in (b) for different val. It is shown as a function of T_{op} for a constant V_{bias} in (c) for different trig and in (d) for different val. For a constant V_{ov} , it is shown as a function of T_{op} in (e) for different trig. Measured with the FDG-filled scatter phantom, it is shown in (f) as a function of activity for different trig and val.

4.3. System Energy Resolution

The exemplary energy spectrum for coincident singles obtained from an measurement with the FDG-filled scatter phantom for an activity of 8.41 MBq with $\Delta E/E = 12.39\%$ is shown in Figure 4.

Using the ^{22}Na sources at the default benchmark point (see Methods 3.3.1), $\Delta E/E$ for trig 2, trig 3 and trig 4 was measured as 12.75 %, 12.75 % and 12.85 %. Increasing the V_{ov} from 2.5 V to 3 V improved $\Delta E/E$ relatively by 1 %–2 % (Figure 5a and Figure 5b).

For constant V_{bias} , decreasing T_C from 15 °C down to –5 °C (T_{op} from ~21 °C down to ~3 °C) improved $\Delta E/E$ relatively by ~ 2.5 %–3.5 % (Figure 5c and Figure 5d). In the evaluated T_{op} range, trig 1 showed an approximately twofold stronger dependence. For constant V_{ov} , the dependence of $\Delta E/E$ on T_{op} was smaller and was measured as a relative change of ~1 % for a comparable change in T_{op} (Figure 5e). $\Delta E/E$ for trig 4 was relatively ~1 % worse compared to trig 2 and 3 for all operating conditions.

$\Delta E/E$ determined with the measurement of the mouse-sized scatter phantom as a function of activity is shown in Figure 5f. It degraded relatively by ~9 % from low activities to 100 MBq for all trig. Trig 1 showed an $\Delta E/E$ which was relatively ~1 % worse compared to the other trig.

4.4. Coincidence Resolution Time

Using the ^{22}Na sources at the default benchmark point (see Methods 3.3.1), the system's CRT using the NE for trig 2, trig 3 and trig 4 was measured as 450 ps, 562 ps and 1.3 ns, respectively. Increasing V_{ov} from 2.5 V to 3 V improved the CRT up to ~9 % (Figure 6a and Figure 6b). Higher val showed a stronger improvement.

For constant V_{bias} , decreasing T_C from 15 °C down to –5 °C (T_{op} from ~21 °C down to ~3 °C) improved the CRT values up to 15 %–20 %. When operating at a T_{op} of 4.48 ± 1.45 °C and 13.41 ± 1.32 °C, trig 1 delivered a CRT of 258 ps and 272 ps (Figure 6c and Figure 6d). For constant V_{ov} , the dependence of CRT on T_{op} was mainly eliminated (Figure 6e). The CRT values measured at $T_C = 15$ °C ($T_{op} \approx 20.5$ °C) were lower than the ones obtained at all other T_{op} . The trig 1 showed a degradation of the CRT value when measuring $T_{op} = 13.77 \pm 1.35$ °C compared to the other T_{op} . The CRT of the WE was 15 %–20 % worse compared to the NE.

Using the mouse-sized scatter phantom, the CRT as a function of activity is shown in Figure 6f. The CRT degraded linearly by about 3 %–5 % from small activities to 100 MBq. Trig 1 showed a more than twofold stronger dependence.

4.5. Sensitivity

The prompts rate for the five ^{22}Na point sources at the default benchmark point (see Methods 3.3.1) was measured as 60 kcps using the NE and 124 kcps for the WE. This results in a sensitivity of 1.0 % and 2.1 % for the given distribution of point sources. Increasing the V_{ov} from 2.5 V to 3 V improved the sensitivity only for trig 4. The other trig lost up to 10 % sensitivity (Figure 7a). For high val increasing the V_{ov} was beneficial. Low val, on the other hand, lost sensitivity (Figure 7b).

For constant V_{bias} , decreasing T_{op} improved the sensitivity for almost all operating parameters. Only the sensitivity for trig 2 to 4 degraded when going from $T_{op} \approx 11.5$ °C to $T_{op} \approx 3.0$ °C and applying the NE (Figure 7c and Figure 7d). For constant

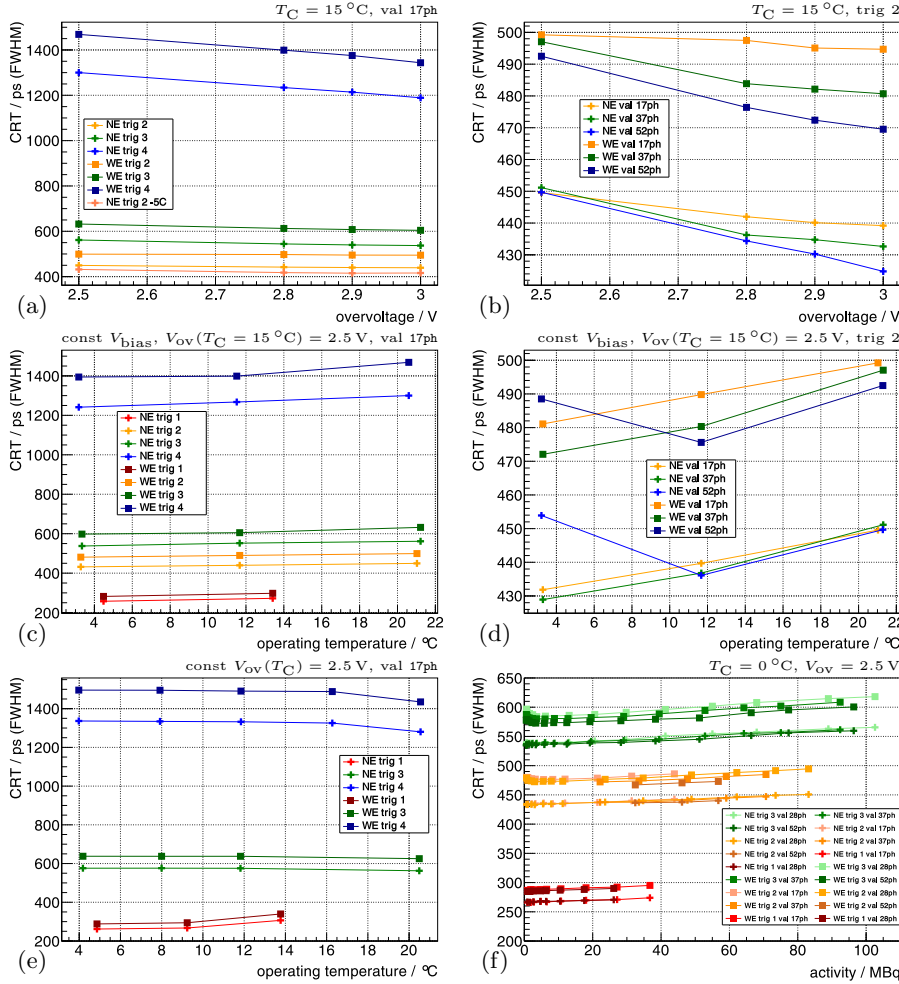


Figure 6. The CRT measured with the ^{22}Na point sources is shown in (a) as a function of V_{ov} for different trig and in (b) for different val. It is shown for a constant V_{bias} as a function of T_{op} in (c) for different trig and in (d) for different val. For a constant V_{ov} , it is shown as a function of T_{op} in (e) for different trig. Measured with the FDG-filled scatter phantom, it is shown in (f) as a function of activity for different trig and val.

V_{ov} , lower T_{op} were beneficial for all trig Figure 7e. Especially the sensitivity of trig 1 was strongly dependent on T_{op} . It showed a loss of $\sim 35\%$ at $T_{\text{op}} = 4.86 \pm 1.42^\circ\text{C}$ up to $\sim 65\%$ at $T_{\text{op}} = 13.77 \pm 1.35^\circ\text{C}$ compared to the higher trig.

Using the mouse-sized scatter phantom, the scatter fraction was measured to be $\sim 6\%$ for the NE and $\sim 16\%$ for the WE. It showed a slight increase as a function of activity (Figure 8a). For the NE it was almost independent of the used trig and val. For the WE, the maximal differences were within a relative band of $\sim \pm 15\%$.

The random fraction of the system was dependent on the used energy window and the CW applied (Figure 8b). It can be roughly approximated with a linear dependence on the activity of $\sim 0.02\%/\text{MBq} - 0.05\%/\text{MBq}$.

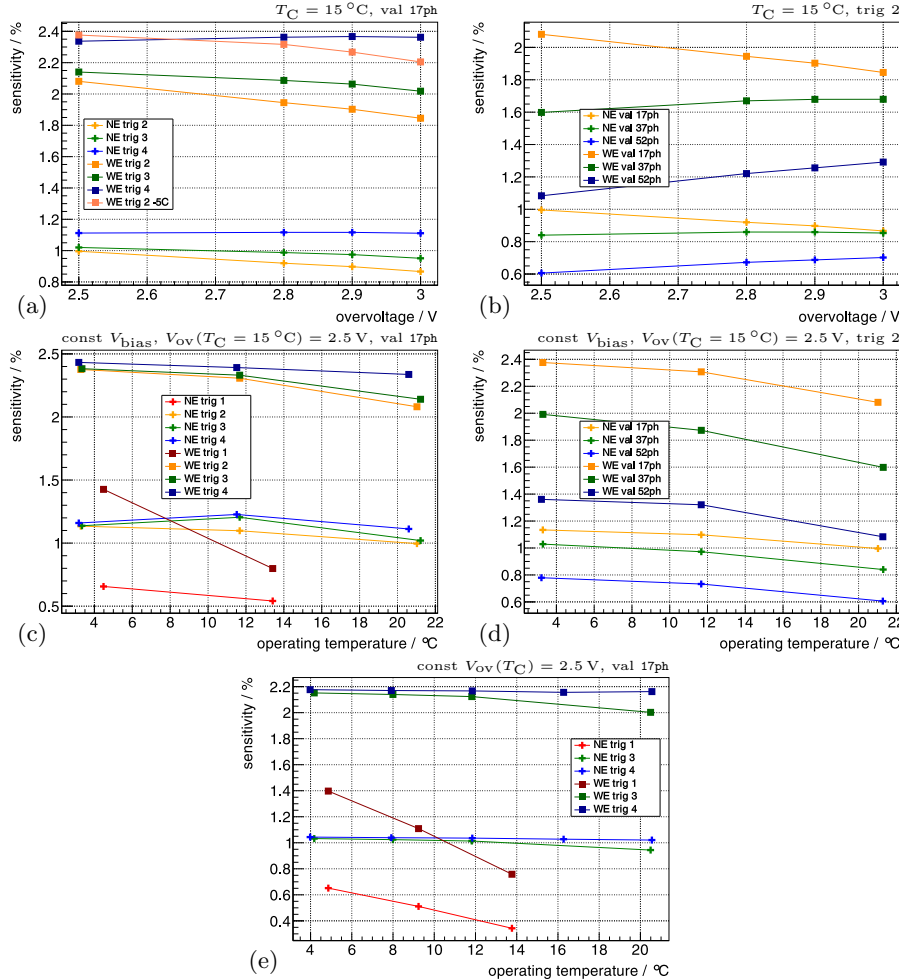


Figure 7. The sensitivity for the ^{22}Na point sources (Table 2) is shown as a function of V_{ov} in (a) for different trig and in (b) for different val. It is shown for a constant V_{bias} as a function of T_{C} in (c) for different trig and in (d) for different val. For a constant V_{ov} , it is shown as a function of T_{C} in (e) for different trig.

The NECR curves of the mouse scatter phantom showed different peak NECRs dependent on the trig and val (Figure 8c). The peak NECR was for all parameters beyond 25 MBq. Using WE, trig 2 and 3 with a val of at least 28ph, we measured peak NECRs of about 280 kcps–320 kcps. For higher trig and val the peak NECR shifted to activities of up to 50 MBq.

The trues sensitivity curve for the mouse scatter phantom is shown in Figure 8d. For low activities, an approximately linear decrease in trues sensitivity could be observed, followed by a stronger decline of the sensitivity.

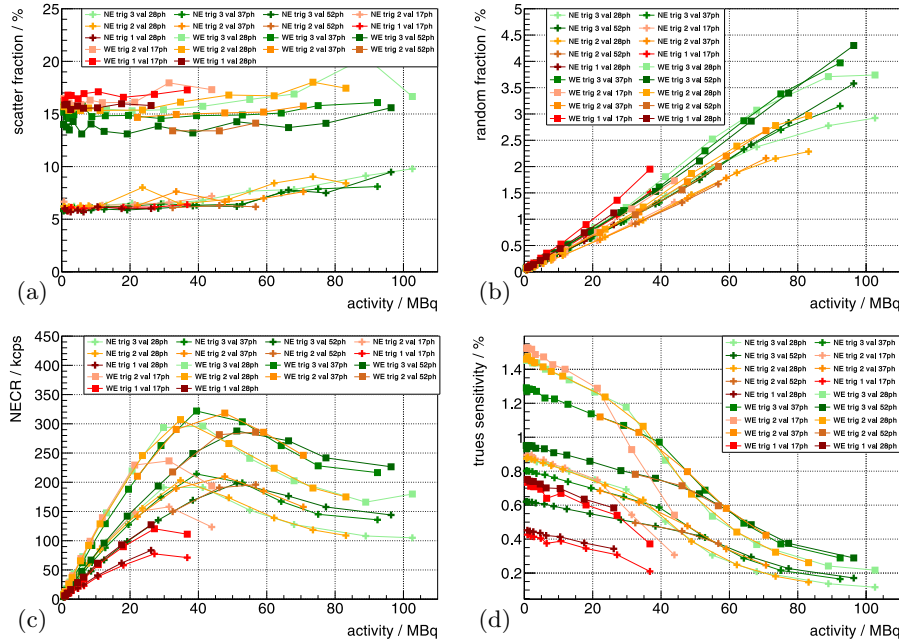


Figure 8. (a) the scatter fraction curves for the mouse scatter phantom for a constant $V_{ov} = 2.5$ V and $T_C = 0$ °C for different trig and val. The two bands for the different energy windows can clearly be distinguished. (b) the random fraction for the mouse scatter phantom for a constant $V_{ov} = 2.5$ V and $T_C = 0$ °C for different trig and val. (c) the NECR curves for the mouse scatter phantom for a constant $V_{ov} = 2.5$ V and $T_C = 0$ °C for different trig and val. (d) the true sensitivity for the same measurements.

4.6. FDG Mouse-Sized Hot-Rod Phantom

The results and statistics for the mouse-sized hot-rod phantom measurements are listed in Table 3. The measurements normalized for the same amount of decays during the measurement time are shown for trig 3 and trig 1 in Figure 9 (a) and (b) and those normalized for the same number of coincidences in Figure 9 (c) and (d). None of the measurements showed a benefit of the TOF reconstruction.

The profile lines through the slices, as defined in Figure 3, are shown for 0.8 mm and 1.0 mm rods in Figure 10a and for 0.9 mm and 1.2 mm rods in Figure 10b. As the profiles did show a systematic dependency of the peak-to-valley values on the position and did not differ significantly for the different measurement settings and reconstructions, we restrict to state a combined mean peak-to-valley value for each rod size of all the shown profiles. The extracted mean peak-to-valley values and their standard deviations are 1.24 ± 0.15 , 1.47 ± 0.18 , 1.87 ± 0.19 and 2.32 ± 0.28 for rod sizes of 0.8 mm, 0.9 mm, 1.0 mm and 1.2 mm, respectively.

4.7. FDG Rabbit-Sized Phantom

For the measurement with the axes of the Cartesian grid of the phantom aligned with the axes of the transversal plane of the scanner, the results and statistics are listed in Table 4. The measurements normalized for the same amount of decays during

Table 3. Statistics for the hot-rod phantom measurement.

trig	normalized to	activity	system T_{op}	meas. time	FDG decays	LORs
(a)	3	all	9.0 MBq	3.52 ± 1.38 °C	762 s	6.48×10^9
(b)	1	decays	7.9 MBq	3.38 ± 1.29 °C	875 s	6.48×10^9
(c)	3	counts	9.0 MBq	3.52 ± 1.38 °C	640 s	5.49×10^9
(d)	1	all	7.9 MBq	3.38 ± 1.29 °C	1160 s	8.41×10^9

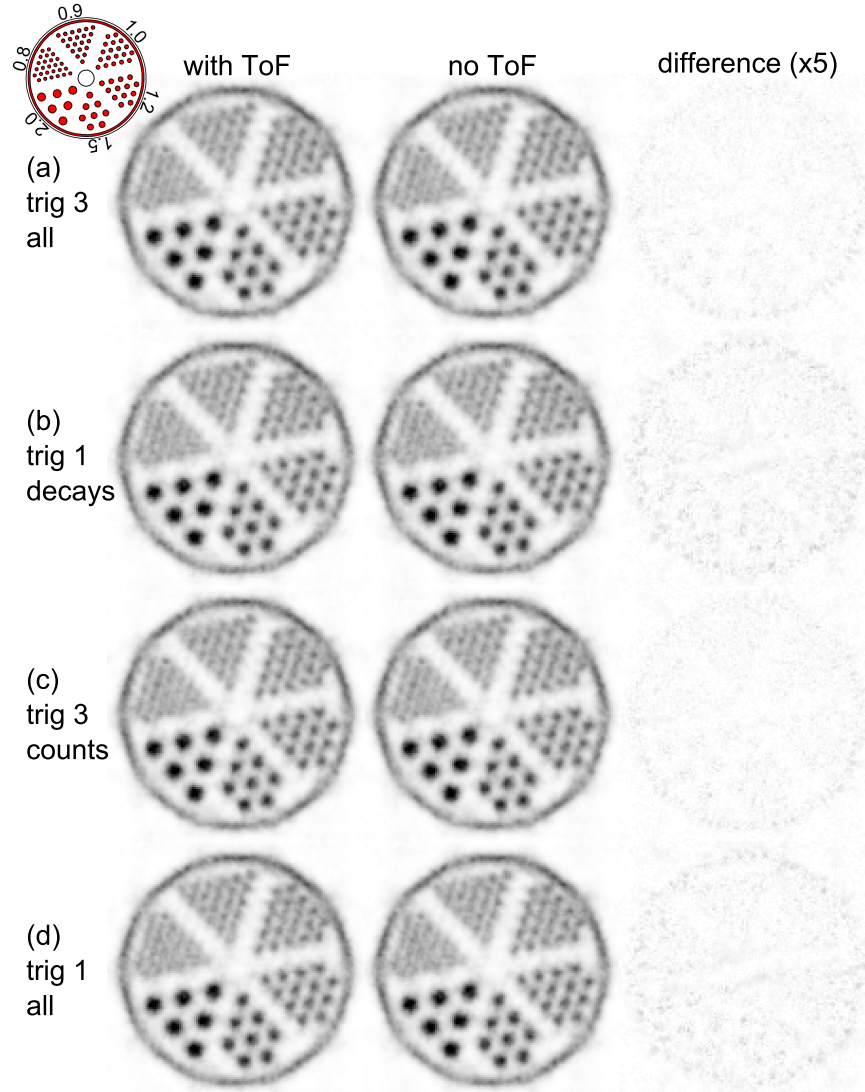


Figure 9. Transversal slices through the reconstructed hot-rod phantom. The voxel pitch is 0.25 mm. The slice thickness is 20 mm. The complete datasets of trig 1 and trig 3 (all) are truncated for comparison: *trig 3 all* matches *trig 1 decays* in terms of the number of tracer decays and *trig 3 counts* matches *trig 1 all* in terms of the number of coincidences (Table 3). The third column shows the absolute difference multiplied with a factor of 5 between the two reconstructions for each measurement.

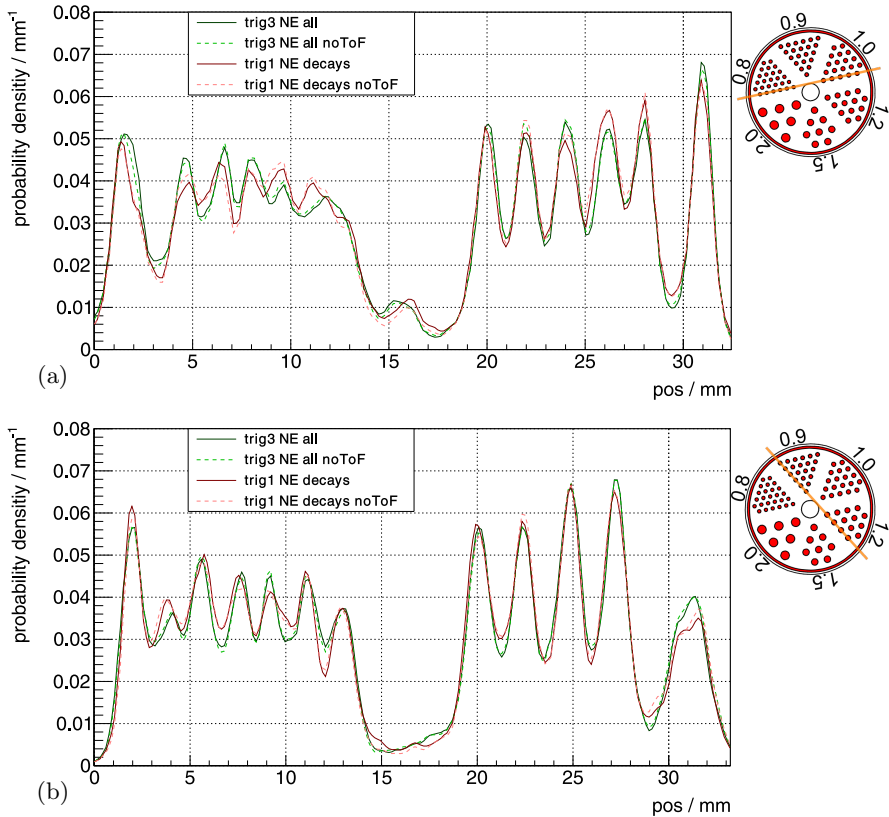


Figure 10. Profiles of the hot-rod phantom through the (a) 0.8 mm and 1.0 mm rods and (b) 0.9 mm and 1.2 mm rods.

the measurement time are shown in Figure 11 (a) and (b) and those normalized for the same number of coincidences in Figure 11 (b) and (c). The untrimmed trig 3 measurement with more than threefold the number of counts compared to the trig 1 is shown in Figure 11 (d).

For the measurement in the tilted position, the results and statistics are listed in Table 5. The measurements normalized for the same amount of decays during the measurement time are shown in Figure 12 (a) and (b) and those normalized for the same number of coincidences in Figure 12 (c) and (d).

For both phantom orientations, the trig 1 measurements (Figure 11 (b), Figure 11 (b) and (d)) showed a benefit of the TOF reconstruction.

5. Discussion

$\Delta E/E$ and CRT are comparable to results shown with similar scintillators on the PDPC TEK platform (Dueppenbecker et al. 2011; Degenhardt et al. 2012). We conclude that the Hyperion-II^D data acquisition platform provides a stable clocking and voltage environment on a system level. In other studies, we showed that our

Table 4. Statistics for the rabbit-sized phantom measurement.

trig	normalized	activity	system T_{op}	meas. time	FDG decays	LORs
(a)	3	decays	3.8 MBq	$3.85 \pm 1.14^\circ\text{C}$	779 s	2.79×10^9
(b)	1	all	3.0 MBq	$4.83 \pm 1.39^\circ\text{C}$	1018 s	2.79×10^9
(c)	3	counts	3.8 MBq	$3.85 \pm 1.14^\circ\text{C}$	478 s	1.75×10^9
(d)	3	all	3.8 MBq	$3.85 \pm 1.14^\circ\text{C}$	1542 s	5.23×10^9

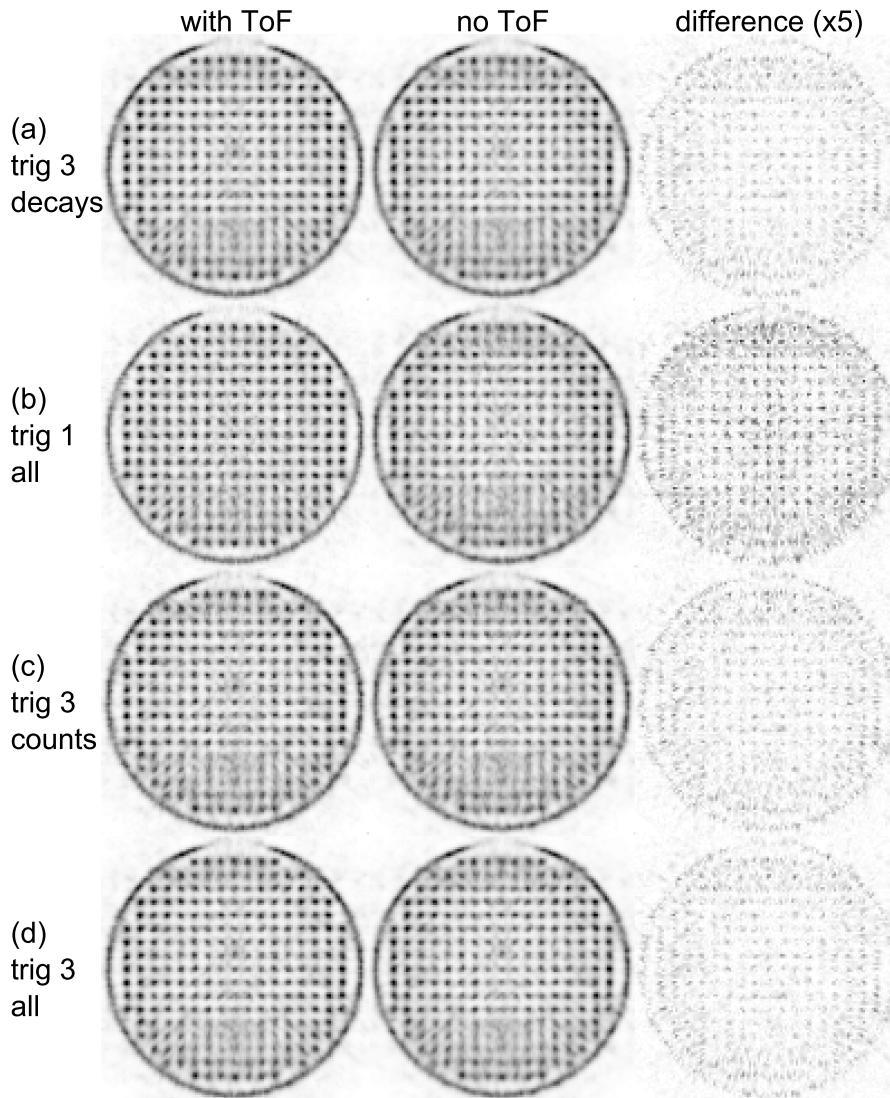


Figure 11. Transversal slices through the reconstructed rabbit-sized phantom. The voxel pitch is 1 mm. The slice thickness is 10 mm. The complete datasets of trig 1 and trig 3 (all) are truncated for comparison: *trig 3 decays* matches *trig 1 all* in terms of the number of tracer decays and *trig 3 counts* matches *trig 1 all* in terms of the number of coincidences (Table 4). The third column shows the absolute difference multiplied with a factor of 5 between the two reconstructions for each measurement.

Table 5. Statistics for the rabbit-sized phantom measurement in the tilted position.

	trig	normalized	activity	system T_{op}	meas. time	FDG decays	LORs
(a)	3	all	11.9 MBq	$3.49 \pm 1.15^\circ\text{C}$	708 s	7.99×10^9	43.47×10^6
(b)	1	decays	13.8 MBq	$3.66 \pm 1.26^\circ\text{C}$	606 s	7.99×10^9	26.70×10^6
(c)	3	counts	11.9 MBq	$3.49 \pm 1.15^\circ\text{C}$	652 s	7.38×10^9	40.10×10^6
(d)	1	all	13.8 MBq	$3.66 \pm 1.26^\circ\text{C}$	924 s	11.89×10^9	40.10×10^6

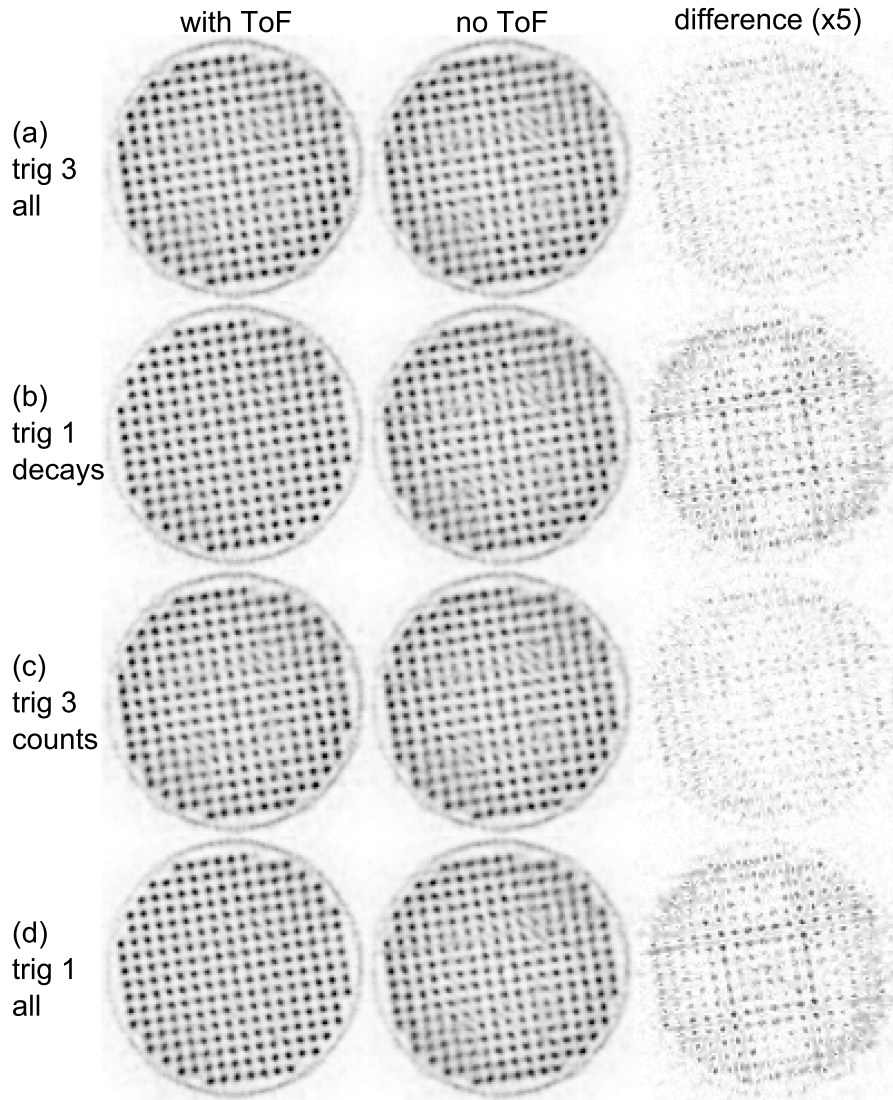


Figure 12. Transversal slices through the reconstructed rabbit-sized phantom measured in the tilted position. The voxel pitch is 1 mm. The slice thickness is 10 mm. The complete datasets of trig 1 and trig 3 (all) are truncated for comparison: *trig 3 all* matches *trig 1 decays* in terms of the number of tracer decays and *trig 3 counts* matches *trig 1 all* in terms of the number of coincidences (Table 5). The third column shows the absolute difference multiplied with a factor of 5 between the two reconstructions for each measurement.

platform is capable of being operated simultaneously inside an MRI (Wehner et al. 2014; Wehner et al. 2015; Schug et al. 2015a; Weissler et al. 2015).

5.1. Possible Operating Parameters

The current limitation on the I_{util} line introduces limitations on the possible operating parameters. High operating temperatures cause high DCRs. In combination with low trig, a high DCR will produce noise triggers which increases the power consumption and dead time of the DPCs. $T_C = 5^\circ\text{C}$ ($T_{\text{op}} = 13.77 \pm 1.35^\circ\text{C}$) was the highest temperature applied using trig 1 which allowed a stable operation. Furthermore, trig 1 was only applicable up to activities of 36.74 MBq due to the current limitation on the I_{util} line. Even without these restrictions, trig 1 should not be used at $T_{\text{op}} \gtrsim 5^\circ\text{C} - 10^\circ\text{C}$ as this introduces significant dead time. The higher trig are more robust to high temperatures but still benefit from low temperatures, especially in terms of sensitivity. Limits of the platform due to the saturation of the GbE interfaces are discussed in section 5.4.

5.2. Energy Resolution

$\Delta E/E$ of $\sim 12.7\%$ was very stable for all combinations of parameters applied. At this level, the scanner outperforms $\Delta E/E$ shown on other preclinical systems (Inveon: 14.6% (Bao et al. 2009), PET Component of the NanoPET/CT: 19% (Szanda et al. 2011), LabPET: 25% (Bergeron et al. 2014)). A good energy resolution allows to discriminate photopeak from scattered events. The temperature dependency was smaller for constant V_{ov} , as expected. The slight degradation towards higher activities can most likely be attributed to pile-up effects.

5.3. Coincidence Resolution Time

The CRT for trig 1 is the best that has been shown for a system with a high-resolution pixelated scintillator configuration so far. However, the CRT values obtained with trig 2 and 3 still outperform, to our knowledge, commercial preclinical systems available today (Inveon: 1.22 ns (Lenox et al. 2006), PET Component of the NanoPET/CT: 1.5 ns – 3.2 ns (Szanda et al. 2011), LabPET: ~ 9 ns (Bergeron et al. 2014)).

Generally, the CRT improved with increasing V_{ov} . The effect was higher for high val as the noise induced DPC hits get a smaller statistical weight when determining the final CRT. The CRT for the WE is expected to be worse as no energy-dependent walk correction for the time stamps was performed.

One measurement with constant V_{bias} at $T_C = -5^\circ\text{C}$ ($T_{\text{op}} = 3.21 \pm 1.15^\circ\text{C}$), $V_{\text{ov}} = 2.5$ V, val 52ph and trig 2 showed a deviation in terms of CRT from the expected behavior (see Figure 6d and Table S1 measurement 11 and 12). Our only explanation is that the configuration of the system was not applied as expected. The measurement with constant V_{ov} at $T_C = 15^\circ\text{C}$ ($T_{\text{op}} \approx 20.5^\circ\text{C}$) showed a better CRT performance than the ones obtained at all other temperatures (see Table S2 measurements 21 – 24). We can only explain this behavior with a faulty determination of V_{bd} at this temperature leading to a different effective V_{ov} compared to the other measurements.

5.4. Sensitivity

A higher V_{ov} increases the PDE of the DPCs as well as the DCR and cross talk. Therefore, increasing the V_{ov} for low val causes more dark noise events to be validated and thus increases the dead time reducing the system's sensitivity. If a high val is applied, not all DPCs of low-energy events may be validated and a higher V_{ov} increases the probability to reach the validation threshold and thus increases the system's sensitivity.

The random fraction measured with the mouse-sized scatter phantom is low compared to commercially available systems (Goertzen et al. 2012). This is due to the superior CRT performance and the resulting possible narrow CW. The scatter fraction measured with the small RF Tx/Rx coil is comparable to the lowest values obtained for other preclinical systems (Goertzen et al. 2012). The slight increase of the determined scatter fraction towards high activities can only be explained by fluctuations in the evaluation method, e.g. random estimation, as the scatter fraction should be independent of the activity.

The NECR peak values strongly depended on the chosen trig and val. For the used raw DPC sensor data mode, the GbE interfaces are the bottleneck of the maximum rate of sensor data, the system was able to deliver. If the limit is reached, hit data is statistically thrown away on individual SDMs which are in saturation. This explains why the system showed a stronger decline of the trues sensitivity and NECR when reaching this limit. Measurements with one or more SDMs in saturation should be avoided as hit data is lost depending on the number of hits recorded per SDM. This can lead to activity-dependent loss rates for SDMs, especially if the activity is not symmetrically distributed around the isocenter of the scanner. Therefore, artifacts in the estimated trues rate, randoms rate, scatter fraction and NECR for measurements with SDMs in saturation are most likely caused by data loss. A peak NECR of ~ 280 kcps – 320 kcps at activities of 30 MBq – 55 MBq delivers good sensitivity for most preclinical applications. Processing and compression of sensor data in firmware should allow to push the peak NECRs to higher values at higher activities until the detector-stack-to-SDM-communication interface or the sensor itself are saturated.

The sensitivity of trig 1 was significantly lower compared to the higher trig for all T_{op} using the COG-ACE crystal identification method. With the employed light sharing, a statistical crystal identification method such as maximum-likelihood estimation could be used to recover the sensitivity loss of trig 1. This, however, would probably occur at the cost of $\Delta E/E$ and CRT performance.

5.5. Image Spatial Resolution and Benefit of TOF

In the 2D slice of the mouse-sized hot-rod phantom, the scanner was able to separate the 0.8 mm rod region, with the exception of the two rods closest to the center of the phantom which were not resolved. All 0.9 mm rods were separable and clearly identifiable. Although not yet determined according to the NEMA NU 4 standard, the spatial resolution of the scanner seems comparable to the best values reported for other preclinical systems (Goertzen et al. 2012). Trig 1 and trig 3 delivered almost the same peak-to-valley value which indicates that the reconstruction was most likely not limited by statistics. Furthermore, no observable benefit of a reconstruction using the TOF information for neither the trig 1 nor the trig 3 measurement could be shown. This is not surprising, as the CRT of trig 1 (~ 260 ps) translates to a spatial resolution

along the LOR of 39 mm which is still larger than the mouse-sized hot-rod phantom. The better CRT may be used to reduce the random fraction at the cost of sensitivity (Eriksson and Conti 2015).

For the rabbit-sized phantom, trig 1 with TOF information showed clear benefit due to the large object diameter. Especially in regions of overlapping horizontal and vertical gaps of the system's geometry that are parallel to the symmetry axes of the Cartesian grid of the phantom, TOF information helped to improve the image quality (Figure 13). Trig 3 did not show an observable improvement when using TOF information for the reconstruction. The trig 3 reconstructions using the complete statistics, which was more than threefold the number of coincidences compared to trig 1, were not able to deliver a comparable image quality to trig 1 with TOF information.

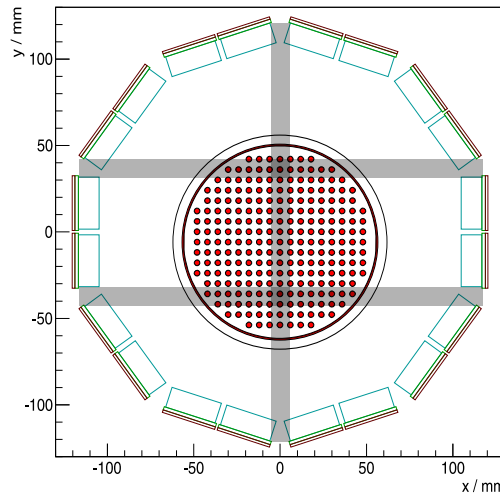


Figure 13. Transversal cross-section through the gantry. The LYSO crystal array outlines are drawn in light blue and the light guide in green. The sensor tile is sketched in red. The rabbit-sized phantom is shown at the measured untilted position which is not centered along the y -axis. In gray are plotted the gaps in horizontal and vertical direction, and parallel to the symmetry axes of the Cartesian grid of the phantom and intersecting the activity distribution.

Even though the rotated phantom measurement showed a more homogeneous image quality over the whole area of the phantom, there are still some artifacts visible around the central region (Figure 12). They are significantly reduced by the trig 1 measurement with TOF information.

The measurements using the rabbit-sized phantom suggest an improvement in image quality by TOF information which cannot be compensated by a non-TOF measurement with higher statistics. The cause might be the non-homogeneous image spatial resolution of the scanner which has a directional dependency. It has to be mentioned that the phantom with rods on a Cartesian grid is a very artificial distribution of activity. A smoother activity distribution containing only some lesions might show a different behavior of the image quality.

A detailed evaluation of the image quality in terms of SNR is ongoing and will be part of the full NEMA NU 4 characterization.

Table 6. Recommended measurement settings when using the Hyperion-II^D scanner to capture the raw DPC sensor data and approximate values for the expected performance.

scenario	$\sim T_{op}$	V_{ov}	trig	val	$\Delta E/E$	CRT	\sim NECR peak
low activity (< 30 MBq)	< 15 °C	2.5 V	2/3	28ph	12.7 %	440 ps/550 ps	280 kcps(40 MBq)
high activity (< 60 MBq)	< 15 °C	2.5 V	2/3	37ph	12.7 %	440 ps/550 ps	300 kcps(55 MBq)
high temperature	< 25 °C	2.5 V	4	28ph	13.0 %	1300 ps	not measured
large object ($\emptyset \gg 40$ mm)	< 10 °C	2.5 V	1	28ph	12.8 %	260 ps	120 kcps(25 MBq)

6. Conclusion

The robust COG-ACE algorithm presented in Schug et al. 2015b was applied to raw DPC sensor data captured with the Hyperion-II^D scanner using a wide range of operating parameters. The system and applied algorithm showed very stable PET performance results under a wide range of operating parameters. The presented initial evaluation of the PET performance results in a good understanding of the system and its behavior under a variety of parameters.

Aggressive voltage settings only have very minor benefits for the energy and timing performance of the system compared to a conservative choice of $V_{ov} = 2.5$ V (relative change < 10 %). Higher voltages can be used to increase the sensitivity for trig 4 and high val. Lower trig and val, on the other hand, lose sensitivity at aggressive voltage settings. We conclude that it is not beneficial to use aggressive $V_{ov} > 2.5$ V for the presented imaging applications.

Low T_{op} are beneficial for all operation parameters. To apply the trig 1, the DPCs should be operated at $T_{op} \lesssim 10$ °C as otherwise the dead time causes a significant loss of sensitivity, especially in the presented application using light sharing. Even lower temperatures are preferable to keep the sensitivity loss at a minimum. Trig 2 and 3 still deliver CRTs of about 440 ps and 550 ps while being more robust to higher temperatures and should be the preferred choice for most preclinical applications. We could show that the CRT of ~ 260 ps for trig 1 does outperform the trig 3 setting for a rabbit-sized activity distribution. For a mouse-sized phantom, the TOF information of trig 1 did not help to improve the image quality noticeably. We conclude that trig 1 should only be the preferred choice if the diameter of the activity distribution is large ($\gg 40$ mm) to benefit from the TOF information.

Using light sharing, one should use low val to increase the probability for all DPCs to be validated that are required for crystal identification (Schug et al. 2015b). On the other hand, low val lead to the generation of many DPC hits and the large amount of data lead to a saturation of the GbE interfaces at activities of about 25 MBq–30 MBq. If high-activity measurements are performed (> 50 MBq–60 MBq), high val give a better NECR performance as the as the current limit given by the GbE interfaces is shifted to higher activities. Compression or processing of raw DPC sensor data on detector stack and/or SDM level will help to remove this bottleneck.

For the Hyperion-II^D scanner in the presented configuration equipped with six detector stacks per SDM and using the raw DPC sensor data mode, we suggest the measurement settings listed in Table 6.

7. Outlook

Based on the findings in this paper, a few sets of parameters will be selected and a scanner characterization following the full NEMA NU 4 standard will be conducted. The TOF benefit will be evaluated in terms of SNR gain using standardized phantoms. The interference study between the Hyperion-II^D platform and a 3-T MRI is ongoing (Wehner et al. 2014; Wehner et al. 2015; Schug et al. 2015a; Weissler et al. 2015).

With the unique possibility to capture raw DPC sensor data, the Hyperion-II^D scanner will allow to study a wide range of different processing methods since they can be implemented in flexible software-based frameworks and will allow to evaluate these methods and their parameters for exactly the same PET measurement.

8. Acknowledgements

This work was supported by the European Community Seventh Framework Programme, project number 241711: SUB nanosecond Leverage In PET/MR ImAging (SUBLIMA).

The project "ForSaTum" is co-funded by the European Union (European Regional Development Fund - Investing in your future) and the German federal state North Rhine-Westphalia (NRW).

The Centre of Excellence in Medical Engineering funded by the Wellcome Trust and EPSRC under grant number WT 088641/Z/09/Z.

The presented work is financially supported by Philips Research Europe, Aachen, Germany.

9. References

Bao, Q., D. Newport, M. Chen, D. B. Stout, and A. F. Chatzioannou (2009). "Performance evaluation of the inveon dedicated PET preclinical tomograph based on the NEMA NU-4 standards." In: *Journal of Nuclear Medicine* 50.3, pp. 401–408. DOI: 10.2967/jnumed.108.056374.

Bergeron, M., J. Cadorette, M.-A. Tetrault, J.-F. Beaudoin, J.-D. Leroux, R. Fontaine, and R. Lecomte (2014). "Imaging performance of LabPET APD-based digital PET scanners for pre-clinical research." In: *Physics in medicine and biology* 59.3, p. 661. DOI: 10.1088/0031-9155/59/3/661.

Buchbender, C., T. A. Heusner, T. C. Lauenstein, A. Bockisch, and G. Antoch (2012a). "Oncologic PET/MRI, part 1: tumors of the brain, head and neck, chest, abdomen, and pelvis." In: *J. Nucl. Med.* 53.6, pp. 928–938. DOI: 10.2967/jnumed.112.105338.

Buchbender, C., T. A. Heusner, T. C. Lauenstein, A. Bockisch, and G. Antoch (2012b). "Oncologic PET/MRI, part 2: bone tumors, soft-tissue tumors, melanoma, and lymphoma." In: *J. Nucl. Med.* 53.8, pp. 1244–1252. DOI: 10.2967/jnumed.112.109306.

Dam, H. T. van, G. Borghi, S. Seifert, and D. R. Schaart (2013). "Sub-200 ps CRT in monolithic scintillator PET detectors using digital SiPM arrays and maximum likelihood interaction time estimation." In: *Physics in Medicine and Biology* 58.10, p. 3243. DOI: 10.1088/0031-9155/58/10/3243.

Dam, H. T. van, S. Seifert, and D. R. Schaart (2012). "The statistical distribution of the number of counted scintillation photons in digital silicon photomultipliers: model and validation." In: *Physics in Medicine and Biology* 57.15, p. 4885. DOI: 10.1088/0031-9155/57/15/4885.

Degenhardt, C., G. Prescher, T. Frach, A. Thon, R. de Gruyter, A. Schmitz, and R. Ballizany (2009). "The digital Silicon Photomultiplier – A novel sensor for the detection of scintillation light." In: *Nuclear Science Symposium Conference Record (NSS/MIC), 2009 IEEE*, pp. 2383–2386. DOI: 10.1109/NSSMIC.2009.5402190.

Degenhardt, C., B. Zwaans, T. Frach, and R. de Gruyter (2010). "Arrays of digital Silicon Photomultipliers – Intrinsic performance and application to scintillator readout." In: *Nuclear Science Symposium Conference Record (NSS/MIC), 2010 IEEE*, pp. 1954–1956. DOI: 10.1109/NSSMIC.2010.5874115.

Degenhardt, C., P. Rodrigues, A. Trindade, B. Zwaans, O. Mühlens, R. Dorscheid, A. Thon, A. Salomon, and T. Frach (2012). "Performance Evaluation of a Prototype Positron Emission Tomography Scanner using Digital Photon Counters (DPC)." In: *Nuclear Science Symposium and Medical Imaging Conference (NSS/MIC), 2012 IEEE*, p. 2820. DOI: 10.1109/NSSMIC.2012.6551643.

Disselhorst, J. A., I. Bezrukov, A. Kolb, C. Parl, and B. J. Pichler (2014). "Principles of PET/MR Imaging." In: *Journal of Nuclear Medicine* 55. Supplement 2, 2S–10S. DOI: 10.2967/jnumed.113.129098.

Drzezga, A., M. Souvatzoglou, M. Eiber, A. J. Beer, S. Fürst, A. Martinez-Möller, S. G. Nekolla, S. Ziegler, C. Ganter, E. J. Rummeny, et al. (2012). "First clinical experience with integrated whole-body PET/MR: comparison to PET/CT in patients with oncologic diagnoses." In: *Journal of Nuclear Medicine* 53.6, pp. 845–855. DOI: 10.2967/jnumed.111.098608.

Dueppenbecker, P., S. Lodomez, R. Haagen, P. Marsden, and V. Schulz (2011). "Investigation of a sub-millimeter resolution PET detector with depth of interaction encoding using digital SiPM single sided readout." In: *Nuclear Science Symposium and Medical Imaging Conference (NSS/MIC), 2011 IEEE*, pp. 2252–2253. DOI: 10.1109/NSSMIC.2011.6152490.

Dueppenbecker, P., J. Wehner, W. Renz, S. Lodomez, D. Truhn, P. Marsden, and V. Schulz (2012a). "Gradient transparent RF housing for simultaneous PET/MRI using carbon fiber composites." In: *Nuclear Science Symposium and Medical Imaging Conference (NSS/MIC), 2012 IEEE*, pp. 3478–3480. DOI: 10.1109/NSSMIC.2012.6551793.

Dueppenbecker, P., B. Weissler, P. Gebhardt, D. Schug, J. Wehner, P. Marsden, and V. Schulz (2012b). "Development of an MRI compatible digital SiPM based PET detector stack for simultaneous preclinical PET/MRI." In: *Nuclear Science Symposium and Medical Imaging Conference (NSS/MIC), 2012 IEEE*, pp. 3481–3483. DOI: 10.1109/NSSMIC.2012.6551794.

Eriksson, L. and M. Conti (2015). "Randoms and TOF gain revisited." In: *Physics in Medicine and Biology* 60.4, p. 1613. DOI: 10.1088/0031-9155/60/4/1613.

España, S., R. Marcinkowski, V. Keereman, S. Vandenberghe, and R. Van Holen (2014). "DigiPET: sub-millimeter spatial resolution small-animal PET imaging using thin monolithic scintillators." In: *Physics in Medicine and Biology* 59.13, p. 3405. DOI: 10.1088/0031-9155/59/13/3405.

Frach, T., G. Prescher, C. Degenhardt, R. de Gruyter, A. Schmitz, and R. Ballizany (2009). "The digital silicon photomultiplier – Principle of operation and intrinsic detector performance." In: *Nuclear Science Symposium Conference Record (NSS/MIC), 2009 IEEE*, pp. 1959–1965. DOI: [10.1109/NSSMIC.2009.5402143](https://doi.org/10.1109/NSSMIC.2009.5402143).

Frach, T., G. Prescher, C. Degenhardt, and B. Zwaans (2010). "The digital silicon photomultiplier – System architecture and performance evaluation." In: *Nuclear Science Symposium Conference Record (NSS/MIC), 2010 IEEE*, pp. 1722–1727. DOI: [10.1109/NSSMIC.2010.5874069](https://doi.org/10.1109/NSSMIC.2010.5874069).

Gebhardt, P., B. Weissler, M. Zinke, F. Kiessling, P. Marsden, and V. Schulz (2012). "FPGA-based singles and coincidences processing pipeline for integrated digital PET/MR detectors." In: *Nuclear Science Symposium and Medical Imaging Conference (NSS/MIC), 2012 IEEE*, pp. 2479–2482. DOI: [10.1109/NSSMIC.2012.6551565](https://doi.org/10.1109/NSSMIC.2012.6551565).

Georgiou, M., G. Borghi, S. V. Spirou, G. Loudos, and D. R. Schaart (2014). "First performance tests of a digital photon counter (DPC) array coupled to a CsI(Tl) crystal matrix for potential use in SPECT." In: *Physics in Medicine and Biology* 59.10, p. 2415. DOI: [10.1088/0031-9155/59/10/2415](https://doi.org/10.1088/0031-9155/59/10/2415).

Goertzen, A. L., Q. Bao, M. Bergeron, E. Blankemeyer, S. Blinder, M. Cañadas, A. F. Chatziiannou, K. Dinelle, E. Elhami, H.-S. Jans, et al. (2012). "NEMA NU 4-2008 comparison of preclinical PET imaging systems." In: *Journal of Nuclear Medicine* 53.8, pp. 1300–1309. DOI: [10.2967/jnumed.111.099382](https://doi.org/10.2967/jnumed.111.099382).

Goldschmidt, B., C. W. Lerche, T. Solf, A. Salomon, F. Kiessling, and V. Schulz (2013). "Towards Software-Based Real-Time Singles and Coincidence Processing of Digital PET Detector Raw Data." In: *Nuclear Science, IEEE Transactions on* 60.3, pp. 1550–1559. DOI: [10.1109/TNS.2013.2252193](https://doi.org/10.1109/TNS.2013.2252193).

Hudson, H. and R. Larkin (1994). "Accelerated image reconstruction using ordered subsets of projection data." In: *Medical Imaging, IEEE Transactions on* 13.4, pp. 601–609. ISSN: 0278-0062. DOI: [10.1109/42.363108](https://doi.org/10.1109/42.363108).

Jadvar, H. and P. M. Colletti (2014). "Competitive advantage of PET/MRI." In: *European journal of radiology* 83.1, pp. 84–94. DOI: [10.1016/j.ejrad.2013.05.028](https://doi.org/10.1016/j.ejrad.2013.05.028).

Lenox, M., B. Atkins, D. Pressley, A. McFarland, D. Newport, and S. Siegel (2006). "Digital time alignment of high resolution PET Inveon block detectors." In: *Nuclear Science Symposium Conference Record, 2006. IEEE*. Vol. 4. IEEE, pp. 2450–2453. DOI: [10.1109/NSSMIC.2006.354407](https://doi.org/10.1109/NSSMIC.2006.354407).

Marcinkowski, R., S. España, R. Van Holen, and S. Vandenberghe (2014). "Optimized light sharing for high-resolution TOF PET detector based on digital silicon photomultipliers." In: *Physics in medicine and biology* 59.23, pp. 7125–7139. DOI: [10.1088/0031-9155/59/23/7125](https://doi.org/10.1088/0031-9155/59/23/7125).

Marcinkowski, R., S. España, R. Van Holen, and S. Vandenberghe (2013). "Effects of dark counts on Digital Silicon Photomultipliers performance." In: *Nuclear Science Symposium and Medical Imaging Conference (NSS/MIC), 2013 IEEE*, pp. 1–6. DOI: [10.1109/NSSMIC.2013.6829323](https://doi.org/10.1109/NSSMIC.2013.6829323).

Miller, M., J. Griesmer, D. Jordan, T. Laurence, R. Muzic, M. Narayanan, D. Natarajamani, K.-H. Su, and S. Wang (2014). "Initial characterization of a prototype digital photon counting PET system." In: *Journal of Nuclear Medicine* 55.supplement 1, pp. 658–658.

Oliver, J. and M. Rafecas (2012). "Singles-prompts-randoms: Estimation of spurious data rates in PET." In: *Nuclear Science Symposium and Medical Imaging Conference (NSS/MIC), 2012 IEEE*. IEEE, pp. 2995–2997. DOI: 10.1109/NSSMIC.2012.6551684.

Philips Digital Photon Counting (2014). *PDPC-TEK User Manual v0.21*.

Pichler, B. J., H. F. Wehrle, and M. S. Judenhofer (2008). "Latest advances in molecular imaging instrumentation." In: *Journal of Nuclear Medicine* 49.Suppl 2, 5S–23S. DOI: 10.2967/jnumed.108.045880.

Salomon, A., A. Goedicke, B. Schweizer, T. Aach, and V. Schulz (2011). "Simultaneous Reconstruction of Activity and Attenuation for PET/MR." In: *Medical Imaging, IEEE Transactions on* 30.3, pp. 804–813. ISSN: 0278-0062. DOI: 10.1109/TMI.2010.2095464.

Salomon, A., B. Goldschmidt, R. Botnar, F. Kiessling, and V. Schulz (2012). "A Self-Normalization Reconstruction Technique for PET Scans Using the Positron Emission Data." In: *Medical Imaging, IEEE Transactions on* 31.12, pp. 2234–2240. ISSN: 0278-0062. DOI: 10.1109/TMI.2012.2213827.

Schneider, F. R., K. Shimazoe, I. Somlai-Schweiger, and S. I. Ziegler (2015). "A PET detector prototype based on digital SiPMs and GAGG scintillators." In: *Physics in Medicine and Biology* 60.4, p. 1667. DOI: 10.1088/0031-9155/60/4/1667.

Schug, D., J. Wehner, P. Dueppenbecker, B. Weissler, P. Gebhardt, B. Goldschmidt, T. Solf, F. Kiessling, and V. Schulz (2015a). "ToF Performance Evaluation of PET Modules With Digital Silicon Photomultiplier Technology During MR Operation." In: *Nuclear Science, IEEE Transactions on* 62.3, pp. 658–663. ISSN: 0018-9499. DOI: 10.1109/TNS.2015.2396295.

Schug, D., J. Wehner, B. Goldschmidt, C. Lerche, P. Dueppenbecker, P. Hallen, B. Weissler, P. Gebhardt, F. Kiessling, and V. Schulz (2015b). "Data Processing for a High Resolution Preclinical PET Detector Based on Philips DPC Digital SiPMs." In: *Nuclear Science, IEEE Transactions on* 62.3, pp. 669–678. ISSN: 0018-9499. DOI: 10.1109/TNS.2015.2420578.

Schug, D., F. Kiessling, and V. Schulz (2013). "Fast and unbiased 3D calibration method of arbitrary scintillator based PET detectors." In: *Nuclear Science Symposium and Medical Imaging Conference (NSS/MIC), 2013 IEEE*, pp. 1–4. DOI: 10.1109/NSSMIC.2013.6829084.

Schulthess, G. K. von and H.-P. W. Schlemmer (2009). "A look ahead: PET/MR versus PET/CT." In: *European journal of nuclear medicine and molecular imaging* 36.1, pp. 3–9. DOI: 10.1007/s00259-008-0940-9.

Seifert, S., G. Van der Lei, H. T. Van Dam, and D. R. Schaart (2013). "First characterization of a digital SiPM based time-of-flight PET detector with 1 mm spatial resolution." In: *Physics in medicine and biology* 58.9, p. 3061. DOI: 10.1088/0031-9155/58/9/3061.

Szanda, I., J. Mackewn, G. Patay, P. Major, K. Sunassee, G. E. Mullen, G. Nemeth, Y. Haemisch, P. J. Blower, and P. K. Marsden (2011). "National Electrical Manufacturers Association NU-4 performance evaluation of the PET component of the NanoPET/CT preclinical PET/CT scanner." In: *Journal of Nuclear Medicine* 52.11, pp. 1741–1747. DOI: 10.2967/jnumed.111.088260.

Tabacchini, V., V. Westerwoudt, G. Borghi, S. Seifert, and D. Schaart (2014). "Probabilities of triggering and validation in a digital silicon photomultiplier." In: *Journal of Instrumentation* 9.06, P06016. DOI: 10.1088/1748-0221/9/06/P06016.

Thon, A. (2012). personal communication. Philips Digital Photo Counting.

Vandenbergh, S. and P. K. Marsden (2015). "PET-MRI: a review of challenges and solutions in the development of integrated multimodality imaging." In: *Physics in Medicine and Biology* 60.4, R115. DOI: 10.1088/0031-9155/60/4/R115.

Wehner, J., B. Weissler, P. M. Dueppenbecker, P. Gebhardt, B. Goldschmidt, D. Schug, F. Kiessling, and V. Schulz (2015). "MR-compatibility assessment of the first preclinical PET-MRI insert equipped with digital silicon photomultipliers." In: *Physics in Medicine and Biology* 60.6, p. 2231. DOI: 10.1088/0031-9155/60/6/2231.

Wehner, J., B. Weissler, P. Dueppenbecker, P. Gebhardt, D. Schug, W. Ruetten, F. Kiessling, and V. Schulz (2014). "PET/MRI insert using digital SiPMs: Investigation of MR-compatibility." In: *Nuclear Instruments and Methods in Physics Research Section A: Accelerators, Spectrometers, Detectors and Associated Equipment* 734, pp. 116–121. DOI: 10.1016/j.nima.2013.08.077.

Weissler, B. et al. (2014). "MR compatibility aspects of a silicon photomultiplier-based PET/RF insert with integrated digitisation." In: *Physics in Medicine and Biology* 59.17, p. 5119. DOI: 10.1088/0031-9155/59/17/5119.

Weissler, B. et al. (2012). "Design Concept of World's First Preclinical PET/MR Insert with Fully Digital Silicon Photomultiplier Technology." In: *Nuclear Science Symposium and Medical Imaging Conference (NSS/MIC), 2012 IEEE*, p. 2113. DOI: 10.1109/NSSMIC.2012.6551484.

Weissler, B. et al. (2015). "A Digital Preclinical PET/MRI Insert and Initial Results." In: *Medical Imaging, IEEE Transactions on* PP.99, pp. 1–1. ISSN: 0278-0062. DOI: 10.1109/TMI.2015.2427993. early access.

Yeom, J. Y., R. Vinke, M. Bieniosek, and C. Levin (2013). "Comparison of end/side scintillator readout with digital-SiPM for ToF PET." In: *Nuclear Science Symposium and Medical Imaging Conference (NSS/MIC), 2013 IEEE*, pp. 1–3. DOI: 10.1109/NSSMIC.2013.6829322.

Zaidi, H. and A. Del Guerra (2011). "An outlook on future design of hybrid PET/MRI systems." In: *Medical physics* 38.10, pp. 5667–5689. DOI: 10.1118/1.3633909.

Supplemental data

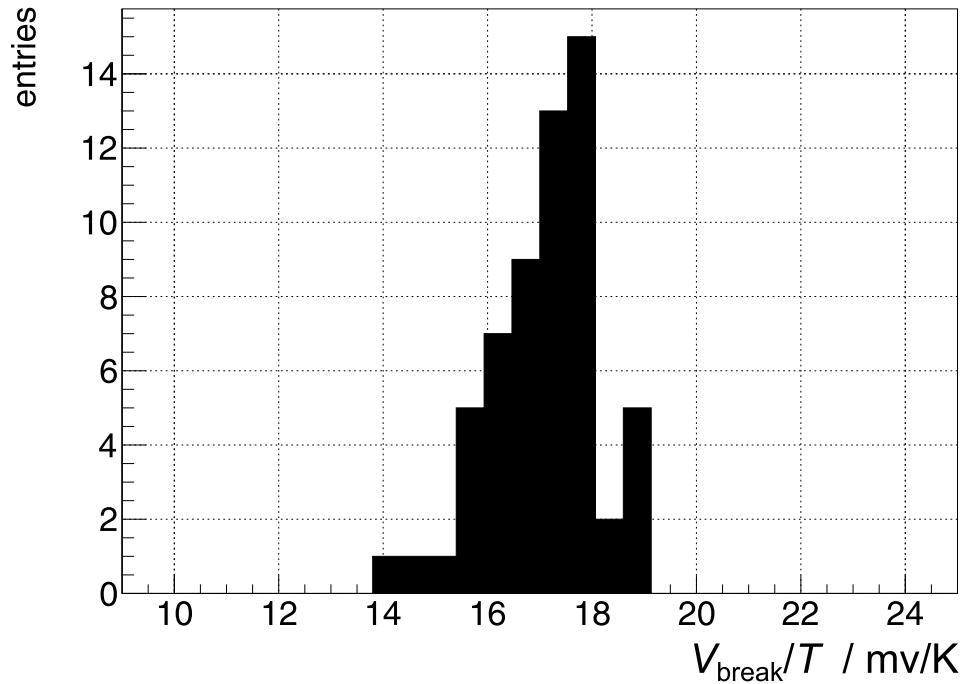


Figure S1. Histogram of the dependence of the breakdown voltage on temperature of all tiles of the system, except for one tile with a faulty temperature sensor.

Table S1: All measurements performed with the 5 ^{22}Na point like sources (distribution and activities listed in Table 2 and constant V_{bias}). A measurement id is used to identify a specific measurement (meas.). The measurement parameters: cooling temperature (T_C), overvoltage (V_{ov}), trigger scheme (trig), validation scheme (val) and the used energy window (EW) are stated for each evaluation of a measurement. The energy resolution and CRT are stated as FWHM and the sensitivity is calculated from the ratio of the prompt rate and the activity of the point sources corrected for the branching ratio of the ^{22}Na β^+ decay of 0.906

meas.	T_C	system T_{op}	V_{ov}	trig	val	EW	$\Delta E/E$	CRT	sens.
1	-5 °C	4.48 ± 1.45 °C	2.5 V	1	17ph	NE	12.45 %	258 ps	0.66 %
2	-5 °C	4.48 ± 1.45 °C	2.5 V	1	17ph	WE	12.47 %	282 ps	1.43 %
3	-5 °C	4.62 ± 1.47 °C	2.8 V	1	17ph	NE	12.74 %	259 ps	0.56 %
4	-5 °C	4.62 ± 1.47 °C	2.8 V	1	17ph	WE	12.75 %	286 ps	1.27 %
5	-5 °C	4.73 ± 1.48 °C	2.9 V	1	17ph	NE	13.86 %	262 ps	0.48 %
6	-5 °C	4.73 ± 1.48 °C	2.9 V	1	17ph	WE	13.92 %	295 ps	1.21 %
7	-5 °C	3.28 ± 1.17 °C	2.5 V	2	17ph	NE	12.39 %	432 ps	1.13 %
8	-5 °C	3.28 ± 1.17 °C	2.5 V	2	17ph	WE	12.40 %	481 ps	2.38 %
9	-5 °C	3.28 ± 1.16 °C	2.5 V	2	37ph	NE	12.40 %	429 ps	1.03 %
10	-5 °C	3.28 ± 1.16 °C	2.5 V	2	37ph	WE	12.42 %	472 ps	1.99 %
11	-5 °C	3.21 ± 1.15 °C	2.5 V	2	52ph	NE	12.35 %	454 ps	0.78 %
12	-5 °C	3.21 ± 1.15 °C	2.5 V	2	52ph	WE	12.36 %	489 ps	1.36 %
13	-5 °C	3.35 ± 1.21 °C	2.8 V	2	17ph	NE	12.32 %	418 ps	1.10 %
14	-5 °C	3.35 ± 1.21 °C	2.8 V	2	17ph	WE	12.34 %	467 ps	2.32 %
15	-5 °C	3.41 ± 1.20 °C	2.9 V	2	17ph	NE	12.31 %	415 ps	1.07 %
16	-5 °C	3.41 ± 1.20 °C	2.9 V	2	17ph	WE	12.33 %	463 ps	2.27 %
17	-5 °C	3.53 ± 1.16 °C	3 V	2	17ph	NE	14.10 %	416 ps	0.93 %
18	-5 °C	3.53 ± 1.16 °C	3 V	2	17ph	WE	14.10 %	467 ps	2.20 %
19	-5 °C	3.34 ± 1.18 °C	2.5 V	3	17ph	NE	12.39 %	538 ps	1.14 %
20	-5 °C	3.34 ± 1.18 °C	2.5 V	3	17ph	WE	12.41 %	598 ps	2.38 %
21	-5 °C	3.17 ± 1.15 °C	2.5 V	4	17ph	NE	12.50 %	1241 ps	1.16 %
22	-5 °C	3.17 ± 1.15 °C	2.5 V	4	17ph	WE	12.55 %	1394 ps	2.43 %
23	5 °C	13.41 ± 1.32 °C	2.5 V	1	17ph	NE	12.81 %	272 ps	0.54 %
24	5 °C	13.41 ± 1.32 °C	2.5 V	1	17ph	WE	12.72 %	298 ps	0.80 %
25	5 °C	11.67 ± 1.05 °C	2.5 V	2	17ph	NE	12.52 %	440 ps	1.10 %
26	5 °C	11.67 ± 1.05 °C	2.5 V	2	17ph	WE	12.56 %	490 ps	2.31 %
27	5 °C	11.67 ± 1.06 °C	2.5 V	2	37ph	NE	12.55 %	437 ps	0.97 %
28	5 °C	11.67 ± 1.06 °C	2.5 V	2	37ph	WE	12.57 %	480 ps	1.87 %
29	5 °C	11.67 ± 1.06 °C	2.5 V	2	52ph	NE	12.58 %	436 ps	0.73 %
30	5 °C	11.67 ± 1.06 °C	2.5 V	2	52ph	WE	12.59 %	476 ps	1.32 %
31	5 °C	11.67 ± 1.06 °C	2.5 V	3	17ph	NE	12.65 %	552 ps	1.20 %
32	5 °C	11.67 ± 1.06 °C	2.5 V	3	17ph	WE	12.57 %	605 ps	2.33 %
33	5 °C	11.51 ± 1.03 °C	2.5 V	4	17ph	NE	12.74 %	1268 ps	1.23 %
34	5 °C	11.51 ± 1.03 °C	2.5 V	4	17ph	WE	12.70 %	1399 ps	2.39 %
35	15 °C	21.03 ± 1.06 °C	2.5 V	2	17ph	NE	12.75 %	450 ps	1.00 %

continued on next page

Table S1 – continued from previous page

meas.	T_C	system T_{op}	V_{ov}	trig	val	EW	$\Delta E/E$	CRT	sens.
36	15 °C	21.03 ± 1.06 °C	2.5 V	2	17ph	WE	12.75 %	499 ps	2.08 %
37	15 °C	21.30 ± 1.10 °C	2.5 V	2	37ph	NE	12.74 %	451 ps	0.84 %
38	15 °C	21.30 ± 1.10 °C	2.5 V	2	37ph	WE	12.78 %	497 ps	1.60 %
39	15 °C	21.28 ± 1.10 °C	2.5 V	2	52ph	NE	12.81 %	450 ps	0.61 %
40	15 °C	21.28 ± 1.10 °C	2.5 V	2	52ph	WE	12.82 %	492 ps	1.08 %
41	15 °C	21.18 ± 1.09 °C	2.8 V	2	17ph	NE	12.63 %	442 ps	0.92 %
42	15 °C	21.18 ± 1.09 °C	2.8 V	2	17ph	WE	12.65 %	497 ps	1.94 %
43	15 °C	21.40 ± 1.13 °C	2.8 V	2	37ph	NE	12.64 %	436 ps	0.86 %
44	15 °C	21.40 ± 1.13 °C	2.8 V	2	37ph	WE	12.66 %	484 ps	1.67 %
45	15 °C	21.36 ± 1.11 °C	2.8 V	2	52ph	NE	12.68 %	434 ps	0.67 %
46	15 °C	21.36 ± 1.11 °C	2.8 V	2	52ph	WE	12.71 %	476 ps	1.22 %
47	15 °C	21.24 ± 1.10 °C	2.9 V	2	17ph	NE	12.62 %	440 ps	0.90 %
48	15 °C	21.24 ± 1.10 °C	2.9 V	2	17ph	WE	12.64 %	495 ps	1.90 %
49	15 °C	21.41 ± 1.13 °C	2.9 V	2	37ph	NE	12.63 %	435 ps	0.86 %
50	15 °C	21.41 ± 1.13 °C	2.9 V	2	37ph	WE	12.65 %	482 ps	1.68 %
51	15 °C	21.40 ± 1.12 °C	2.9 V	2	52ph	NE	12.64 %	430 ps	0.69 %
52	15 °C	21.40 ± 1.12 °C	2.9 V	2	52ph	WE	12.66 %	472 ps	1.26 %
53	15 °C	21.31 ± 1.12 °C	3 V	2	17ph	NE	12.60 %	439 ps	0.87 %
54	15 °C	21.31 ± 1.12 °C	3 V	2	17ph	WE	12.62 %	495 ps	1.85 %
55	15 °C	21.47 ± 1.14 °C	3 V	2	37ph	NE	12.60 %	433 ps	0.85 %
56	15 °C	21.47 ± 1.14 °C	3 V	2	37ph	WE	12.62 %	481 ps	1.68 %
57	15 °C	21.47 ± 1.13 °C	3 V	2	52ph	NE	12.62 %	425 ps	0.70 %
58	15 °C	21.47 ± 1.13 °C	3 V	2	52ph	WE	12.64 %	470 ps	1.29 %
59	15 °C	21.22 ± 1.07 °C	2.5 V	3	17ph	NE	12.74 %	562 ps	1.02 %
60	15 °C	21.22 ± 1.07 °C	2.5 V	3	17ph	WE	12.76 %	632 ps	2.14 %
61	15 °C	21.25 ± 1.07 °C	2.8 V	3	17ph	NE	12.64 %	544 ps	0.99 %
62	15 °C	21.25 ± 1.07 °C	2.8 V	3	17ph	WE	12.67 %	613 ps	2.09 %
63	15 °C	21.29 ± 1.08 °C	2.9 V	3	17ph	NE	12.62 %	540 ps	0.97 %
64	15 °C	21.29 ± 1.08 °C	2.9 V	3	17ph	WE	12.65 %	608 ps	2.06 %
65	15 °C	21.33 ± 1.09 °C	3 V	3	17ph	NE	12.60 %	537 ps	0.95 %
66	15 °C	21.33 ± 1.09 °C	3 V	3	17ph	WE	12.62 %	604 ps	2.02 %
67	15 °C	20.60 ± 0.95 °C	2.5 V	4	17ph	NE	12.85 %	1300 ps	1.11 %
68	15 °C	20.60 ± 0.95 °C	2.5 V	4	17ph	WE	12.88 %	1469 ps	2.34 %
69	15 °C	20.66 ± 0.97 °C	2.8 V	4	17ph	NE	12.75 %	1234 ps	1.12 %
70	15 °C	20.66 ± 0.97 °C	2.8 V	4	17ph	WE	12.78 %	1399 ps	2.36 %
71	15 °C	20.73 ± 0.99 °C	2.9 V	4	17ph	NE	12.73 %	1214 ps	1.12 %
72	15 °C	20.73 ± 0.99 °C	2.9 V	4	17ph	WE	12.76 %	1375 ps	2.37 %
73	15 °C	20.79 ± 0.99 °C	3 V	4	17ph	NE	12.69 %	1189 ps	1.11 %
74	15 °C	20.79 ± 0.99 °C	3 V	4	17ph	WE	12.72 %	1344 ps	2.36 %

Table S2: All measurements performed with the 5 ^{22}Na point like sources (distribution and activities listed in Table 2 and constant V_{ov}). A measurement id is used to identify a specific measurement (meas.). The measurement parameters: cooling temperature (T_C), system operating temperature (T_{op}), overvoltage (V_{ov}), trigger scheme (trig), validation scheme (val) and the used energy window (EW) are stated for each evaluation of a measurement. The energy resolution and CRT are stated as FWHM and the sensitivity is calculated from the ratio of the prompt rate and the activity of the point sources corrected for the branching ratio of the ^{22}Na β^+ decay of 0.906

meas.	T_C	system	T_{op}	V_{ov}	trig	val	EW	$\Delta E/E$	CRT	sens.
1	-5 °C	4.86 ± 1.42 °C	2.5 V	1	17ph	NE	12.62 %	262 ps	0.65 %	
2	-5 °C	4.86 ± 1.42 °C	2.5 V	1	17ph	WE	12.62 %	288 ps	1.40 %	
3	-5 °C	4.18 ± 1.27 °C	2.5 V	3	17ph	NE	12.57 %	576 ps	1.03 %	
4	-5 °C	4.18 ± 1.27 °C	2.5 V	3	17ph	WE	12.57 %	638 ps	2.15 %	
5	-5 °C	3.98 ± 1.24 °C	2.5 V	4	17ph	NE	12.69 %	1336 ps	1.04 %	
6	-5 °C	3.98 ± 1.24 °C	2.5 V	4	17ph	WE	12.71 %	1496 ps	2.18 %	
7	0 °C	9.24 ± 1.44 °C	2.5 V	1	17ph	NE	12.69 %	267 ps	0.51 %	
8	0 °C	9.24 ± 1.44 °C	2.5 V	1	17ph	WE	12.69 %	294 ps	1.11 %	
9	0 °C	8.00 ± 1.12 °C	2.5 V	3	17ph	NE	12.62 %	576 ps	1.02 %	
10	0 °C	8.00 ± 1.12 °C	2.5 V	3	17ph	WE	12.62 %	637 ps	2.14 %	
11	0 °C	7.92 ± 1.11 °C	2.5 V	4	17ph	NE	12.74 %	1334 ps	1.04 %	
12	0 °C	7.92 ± 1.11 °C	2.5 V	4	17ph	WE	12.76 %	1495 ps	2.17 %	
13	5 °C	13.77 ± 1.35 °C	2.5 V	1	17ph	NE	12.77 %	307 ps	0.34 %	
14	5 °C	13.77 ± 1.35 °C	2.5 V	1	17ph	WE	12.77 %	340 ps	0.76 %	
15	5 °C	11.82 ± 0.97 °C	2.5 V	3	17ph	NE	12.66 %	575 ps	1.01 %	
16	5 °C	11.82 ± 0.97 °C	2.5 V	3	17ph	WE	12.67 %	637 ps	2.12 %	
17	5 °C	11.85 ± 0.99 °C	2.5 V	4	17ph	NE	12.79 %	1332 ps	1.04 %	
18	5 °C	11.85 ± 0.99 °C	2.5 V	4	17ph	WE	12.80 %	1491 ps	2.17 %	
19	10 °C	16.27 ± 0.95 °C	2.5 V	4	17ph	NE	12.84 %	1326 ps	1.03 %	
20	10 °C	16.27 ± 0.95 °C	2.5 V	4	17ph	WE	12.86 %	1488 ps	2.16 %	
21	15 °C	20.49 ± 0.85 °C	2.5 V	3	17ph	NE	12.72 %	563 ps	0.94 %	
22	15 °C	20.49 ± 0.85 °C	2.5 V	3	17ph	WE	12.72 %	625 ps	2.00 %	
23	15 °C	20.56 ± 0.88 °C	2.5 V	4	17ph	NE	12.84 %	1280 ps	1.02 %	
24	15 °C	20.56 ± 0.88 °C	2.5 V	4	17ph	WE	12.85 %	1435 ps	2.16 %	

Table S3: All measurements performed with the mouse-sized scatter phantom. A measurement id is used to identify a specific measurement (meas.). The measurement parameters: source activity (activity), system operating temperature (T_{op}) for a cooling temperature of $T_C = 0^\circ\text{C}$, trigger scheme (trig), validation scheme (val) and the used energy window (EW) are stated for each evaluation of a measurement. The energy resolution and CRT are stated as FWHM. The prompt rate (prompts), random fraction (randoms), scatter fraction (scatter), trues sensitivity (sens) and NECR are evaluated following the NEMA NU4 standard.

meas.	activity	system T_{op}	trig	val	EW	$\Delta E/E$	CRT	prompts	randoms	scatter	sens	NECR
1	102.60 MBq	$9.23 \pm 1.35^\circ\text{C}$	3	28ph	NE	13.60 %	566 ps	136.18 kcps	2.92 %	9.79 %	0.12 %	105.04 kcps
2	102.60 MBq	$9.23 \pm 1.35^\circ\text{C}$	3	28ph	WE	13.64 %	618 ps	276.03 kcps	3.74 %	16.66 %	0.22 %	179.88 kcps
3	96.37 MBq	$9.00 \pm 1.32^\circ\text{C}$	3	52ph	NE	13.46 %	560 ps	187.82 kcps	3.58 %	9.48 %	0.17 %	144.06 kcps
4	96.37 MBq	$9.00 \pm 1.32^\circ\text{C}$	3	52ph	WE	13.48 %	600 ps	342.48 kcps	4.30 %	15.59 %	0.29 %	226.48 kcps
5	92.40 MBq	$8.98 \pm 1.32^\circ\text{C}$	3	37ph	NE	13.44 %	561 ps	170.55 kcps	3.15 %	8.10 %	0.16 %	135.79 kcps
6	92.40 MBq	$8.98 \pm 1.32^\circ\text{C}$	3	37ph	WE	13.50 %	609 ps	329.22 kcps	3.97 %	16.09 %	0.29 %	216.54 kcps
7	88.96 MBq	$8.97 \pm 1.32^\circ\text{C}$	3	28ph	NE	13.43 %	563 ps	137.80 kcps	2.78 %	9.13 %	0.14 %	108.11 kcps
8	88.96 MBq	$8.97 \pm 1.32^\circ\text{C}$	3	28ph	WE	13.46 %	615 ps	278.19 kcps	3.71 %	20.39 %	0.24 %	165.98 kcps
9	83.16 MBq	$9.23 \pm 1.36^\circ\text{C}$	2	28ph	NE	13.48 %	451 ps	135.51 kcps	2.29 %	8.41 %	0.15 %	108.97 kcps
10	83.16 MBq	$9.23 \pm 1.36^\circ\text{C}$	2	28ph	WE	13.50 %	495 ps	269.84 kcps	2.97 %	17.45 %	0.26 %	174.93 kcps
11	77.32 MBq	$8.77 \pm 1.28^\circ\text{C}$	3	52ph	NE	13.25 %	556 ps	194.38 kcps	2.84 %	7.49 %	0.23 %	157.70 kcps
12	77.32 MBq	$8.77 \pm 1.28^\circ\text{C}$	3	52ph	WE	13.27 %	595 ps	347.76 kcps	3.40 %	14.11 %	0.37 %	241.72 kcps
13	75.04 MBq	$8.65 \pm 1.26^\circ\text{C}$	3	37ph	NE	13.24 %	557 ps	179.94 kcps	2.70 %	7.88 %	0.22 %	145.19 kcps
14	75.04 MBq	$8.65 \pm 1.26^\circ\text{C}$	3	37ph	WE	13.26 %	602 ps	340.96 kcps	3.38 %	15.79 %	0.37 %	228.12 kcps
15	73.51 MBq	$8.69 \pm 1.26^\circ\text{C}$	2	28ph	NE	13.24 %	449 ps	149.02 kcps	2.15 %	9.04 %	0.18 %	118.51 kcps
16	73.51 MBq	$8.69 \pm 1.26^\circ\text{C}$	2	28ph	WE	13.27 %	491 ps	296.33 kcps	2.78 %	18.02 %	0.32 %	190.14 kcps
17	70.70 MBq	$8.79 \pm 1.29^\circ\text{C}$	2	37ph	NE	13.21 %	447 ps	192.42 kcps	2.16 %	7.61 %	0.25 %	157.74 kcps

continued on next page

Table S3 – continued from previous page

meas.	activity	system	T_{op}	trig	val	EW	$\Delta E/E$	CRT	prompts	randoms	scatter	sens	NECR
18	70.70 MBq	8.79 ± 1.29 °C	2	37ph	WE	13.24 %	485 ps	363.07 kcps	2.68 %	15.75 %	0.42 %	246.12 kcps	
19	67.99 MBq	8.69 ± 1.27 °C	3	28ph	NE	13.18 %	557 ps	157.13 kcps	2.37 %	7.82 %	0.21 %	127.71 kcps	
20	67.99 MBq	8.69 ± 1.27 °C	3	28ph	WE	13.21 %	608 ps	308.95 kcps	3.07 %	16.90 %	0.37 %	202.56 kcps	
21	66.38 MBq	8.60 ± 1.26 °C	3	52ph	NE	13.08 %	551 ps	216.94 kcps	2.42 %	7.78 %	0.29 %	176.36 kcps	
22	66.38 MBq	8.60 ± 1.26 °C	3	52ph	WE	13.09 %	591 ps	382.48 kcps	2.86 %	13.71 %	0.48 %	270.85 kcps	
23	64.23 MBq	8.56 ± 1.25 °C	3	37ph	NE	13.10 %	555 ps	204.15 kcps	2.33 %	7.51 %	0.29 %	167.19 kcps	
24	64.23 MBq	8.56 ± 1.25 °C	3	37ph	WE	13.13 %	599 ps	382.91 kcps	2.87 %	15.09 %	0.49 %	262.72 kcps	
25	62.17 MBq	8.62 ± 1.25 °C	2	28ph	NE	13.11 %	447 ps	171.67 kcps	1.88 %	8.42 %	0.25 %	139.03 kcps	
26	62.17 MBq	8.62 ± 1.25 °C	2	28ph	WE	13.14 %	488 ps	336.41 kcps	2.39 %	16.73 %	0.44 %	224.05 kcps	
27	59.08 MBq	8.55 ± 1.24 °C	2	37ph	NE	13.04 %	444 ps	221.02 kcps	1.78 %	6.98 %	0.34 %	184.96 kcps	
28	59.08 MBq	8.55 ± 1.24 °C	2	37ph	WE	13.06 %	481 ps	412.23 kcps	2.20 %	15.18 %	0.58 %	285.56 kcps	
29	56.76 MBq	8.59 ± 1.25 °C	2	52ph	NE	12.98 %	440 ps	229.72 kcps	1.67 %	6.18 %	0.37 %	195.92 kcps	
30	56.76 MBq	8.59 ± 1.25 °C	2	52ph	WE	13.00 %	473 ps	401.07 kcps	2.00 %	14.13 %	0.60 %	285.64 kcps	
31	55.02 MBq	8.48 ± 1.23 °C	3	28ph	NE	13.02 %	554 ps	185.37 kcps	1.98 %	7.67 %	0.31 %	152.28 kcps	
32	55.02 MBq	8.48 ± 1.23 °C	3	28ph	WE	13.05 %	602 ps	359.67 kcps	2.52 %	16.38 %	0.54 %	240.95 kcps	
33	52.85 MBq	8.34 ± 1.21 °C	3	37ph	NE	12.95 %	551 ps	235.52 kcps	1.86 %	6.43 %	0.41 %	199.06 kcps	
34	52.85 MBq	8.34 ± 1.21 °C	3	37ph	WE	12.97 %	594 ps	435.97 kcps	2.30 %	14.90 %	0.69 %	303.46 kcps	
35	51.24 MBq	8.29 ± 1.20 °C	3	52ph	NE	12.89 %	545 ps	233.09 kcps	1.75 %	6.21 %	0.42 %	198.34 kcps	
36	51.24 MBq	8.29 ± 1.20 °C	3	52ph	WE	12.90 %	582 ps	406.00 kcps	2.11 %	14.27 %	0.67 %	287.71 kcps	
37	48.90 MBq	8.42 ± 1.22 °C	2	28ph	NE	12.96 %	443 ps	205.72 kcps	1.47 %	6.89 %	0.39 %	173.49 kcps	
38	48.90 MBq	8.42 ± 1.22 °C	2	28ph	WE	12.98 %	484 ps	396.89 kcps	1.87 %	16.80 %	0.66 %	266.24 kcps	
39	47.72 MBq	8.37 ± 1.21 °C	2	37ph	NE	12.87 %	441 ps	247.20 kcps	1.40 %	6.66 %	0.48 %	209.80 kcps	
40	47.72 MBq	8.37 ± 1.21 °C	2	37ph	WE	12.91 %	477 ps	454.80 kcps	1.71 %	15.10 %	0.80 %	318.34 kcps	
41	46.13 MBq	8.34 ± 1.21 °C	2	52ph	NE	12.82 %	438 ps	222.72 kcps	1.32 %	6.30 %	0.45 %	190.73 kcps	
42	46.13 MBq	8.34 ± 1.21 °C	2	52ph	WE	12.84 %	471 ps	385.62 kcps	1.56 %	13.40 %	0.71 %	281.45 kcps	
43	43.91 MBq	8.38 ± 1.21 °C	2	17ph	NE	12.90 %	443 ps	146.90 kcps	1.32 %	7.19 %	0.31 %	123.44 kcps	
44	43.91 MBq	8.38 ± 1.21 °C	2	17ph	WE	12.92 %	486 ps	291.54 kcps	1.73 %	17.31 %	0.54 %	193.66 kcps	

continued on next page

Table S3 – continued from previous page

meas.	activity	system	T_{op}	trig	val	EW	$\Delta E/E$	CRT	prompts	randoms	scatter	sens	NECR
45	41.28 MBq	8.29 ± 1.20 °C	3	28ph	NE	12.82 %	551 ps	226.03 kcps	1.44 %	6.78 %	0.50 %	191.21 kcps	
46	41.28 MBq	8.29 ± 1.20 °C	3	28ph	WE	12.84 %	596 ps	429.92 kcps	1.81 %	15.73 %	0.86 %	296.06 kcps	
47	39.46 MBq	8.23 ± 1.18 °C	3	37ph	NE	12.76 %	545 ps	250.26 kcps	1.32 %	6.33 %	0.59 %	214.18 kcps	
48	39.46 MBq	8.23 ± 1.18 °C	3	37ph	WE	12.78 %	589 ps	456.30 kcps	1.61 %	14.84 %	0.97 %	321.89 kcps	
49	38.37 MBq	8.17 ± 1.17 °C	3	52ph	NE	12.73 %	542 ps	197.36 kcps	1.29 %	6.26 %	0.48 %	169.24 kcps	
50	38.37 MBq	8.17 ± 1.17 °C	3	52ph	WE	12.75 %	579 ps	339.67 kcps	1.53 %	13.20 %	0.76 %	249.16 kcps	
51	36.74 MBq	9.37 ± 1.36 °C	1	17ph	NE	13.00 %	274 ps	83.50 kcps	1.52 %	6.38 %	0.21 %	71.12 kcps	
52	36.74 MBq	9.37 ± 1.36 °C	1	17ph	WE	13.02 %	295 ps	167.90 kcps	1.95 %	17.29 %	0.37 %	111.18 kcps	
53	34.77 MBq	8.52 ± 1.28 °C	2	28ph	NE	12.76 %	440 ps	236.51 kcps	0.98 %	6.44 %	0.63 %	203.22 kcps	
54	34.77 MBq	8.52 ± 1.28 °C	2	28ph	WE	12.78 %	479 ps	445.86 kcps	1.23 %	16.12 %	1.06 %	307.22 kcps	
55	33.51 MBq	8.26 ± 1.21 °C	2	37ph	NE	12.69 %	437 ps	225.77 kcps	0.95 %	7.63 %	0.62 %	189.28 kcps	
56	33.51 MBq	8.26 ± 1.21 °C	2	37ph	WE	12.71 %	474 ps	409.27 kcps	1.14 %	14.96 %	1.03 %	290.29 kcps	
57	32.46 MBq	8.16 ± 1.19 °C	2	52ph	NE	12.69 %	436 ps	172.74 kcps	0.91 %	6.09 %	0.50 %	149.74 kcps	
58	32.46 MBq	8.16 ± 1.19 °C	2	52ph	WE	12.70 %	467 ps	295.73 kcps	1.08 %	13.40 %	0.78 %	217.63 kcps	
59	31.41 MBq	8.16 ± 1.17 °C	2	17ph	NE	12.71 %	440 ps	184.16 kcps	0.92 %	6.58 %	0.54 %	157.97 kcps	
60	31.41 MBq	8.16 ± 1.17 °C	2	17ph	WE	12.73 %	482 ps	358.45 kcps	1.19 %	17.96 %	0.93 %	236.57 kcps	
61	29.79 MBq	8.09 ± 1.16 °C	3	28ph	NE	12.66 %	544 ps	222.62 kcps	0.98 %	6.49 %	0.69 %	191.12 kcps	
62	29.79 MBq	8.09 ± 1.16 °C	3	28ph	WE	12.67 %	591 ps	418.93 kcps	1.22 %	15.40 %	1.18 %	293.64 kcps	
63	29.06 MBq	8.03 ± 1.15 °C	3	37ph	NE	12.62 %	543 ps	203.13 kcps	0.96 %	6.46 %	0.65 %	174.56 kcps	
64	29.06 MBq	8.03 ± 1.15 °C	3	37ph	WE	12.64 %	584 ps	367.40 kcps	1.16 %	14.57 %	1.07 %	262.84 kcps	
65	28.24 MBq	8.01 ± 1.14 °C	3	52ph	NE	12.61 %	540 ps	155.82 kcps	0.94 %	6.03 %	0.51 %	135.18 kcps	
66	28.24 MBq	8.01 ± 1.14 °C	3	52ph	WE	12.63 %	577 ps	265.96 kcps	1.13 %	13.85 %	0.80 %	193.59 kcps	
67	27.13 MBq	9.12 ± 1.32 °C	1	17ph	NE	12.84 %	271 ps	89.82 kcps	1.06 %	6.15 %	0.31 %	77.54 kcps	
68	27.13 MBq	9.12 ± 1.32 °C	1	17ph	WE	12.85 %	292 ps	178.30 kcps	1.36 %	16.86 %	0.54 %	120.46 kcps	
69	26.16 MBq	9.44 ± 1.42 °C	1	28ph	NE	12.83 %	271 ps	96.26 kcps	0.89 %	6.01 %	0.34 %	83.61 kcps	
70	26.16 MBq	9.44 ± 1.42 °C	1	28ph	WE	12.84 %	290 ps	183.02 kcps	1.12 %	15.80 %	0.58 %	127.31 kcps	
71	23.63 MBq	8.05 ± 1.16 °C	2	28ph	NE	12.58 %	438 ps	185.62 kcps	0.66 %	8.01 %	0.72 %	155.15 kcps	

continued on next page

Table S3 – continued from previous page

meas.	activity	system	T_{op}	trig	val	EW	$\Delta E/E$	CRT	prompts	randoms	scatter	sens	NECR
72	23.63 MBq	8.05 ± 1.16 °C	2	28ph	WE	12.59 %	477 ps	347.87 kcps	0.81 %	15.38 %	1.24 %	245.69 kcps	
73	22.16 MBq	8.03 ± 1.15 °C	2	37ph	NE	12.55 %	437 ps	162.77 kcps	0.61 %	6.30 %	0.68 %	141.28 kcps	
74	22.16 MBq	8.03 ± 1.15 °C	2	37ph	WE	12.59 %	472 ps	292.57 kcps	0.74 %	14.67 %	1.12 %	210.32 kcps	
75	21.36 MBq	8.03 ± 1.15 °C	2	17ph	NE	12.57 %	437 ps	171.76 kcps	0.59 %	6.38 %	0.75 %	148.87 kcps	
76	21.36 MBq	8.03 ± 1.15 °C	2	17ph	WE	12.59 %	479 ps	330.28 kcps	0.75 %	16.12 %	1.29 %	229.42 kcps	
77	20.60 MBq	7.95 ± 1.14 °C	3	28ph	NE	12.56 %	542 ps	166.22 kcps	0.67 %	6.52 %	0.75 %	143.42 kcps	
78	20.60 MBq	7.95 ± 1.14 °C	3	28ph	WE	12.57 %	588 ps	310.16 kcps	0.84 %	15.30 %	1.27 %	219.35 kcps	
79	19.55 MBq	7.95 ± 1.14 °C	3	37ph	NE	12.52 %	542 ps	146.88 kcps	0.64 %	6.22 %	0.70 %	127.63 kcps	
80	19.55 MBq	7.95 ± 1.14 °C	3	37ph	WE	12.53 %	582 ps	263.01 kcps	0.79 %	14.86 %	1.14 %	188.10 kcps	
81	19.18 MBq	7.87 ± 1.12 °C	3	52ph	NE	12.52 %	539 ps	112.74 kcps	0.63 %	5.88 %	0.55 %	98.68 kcps	
82	19.18 MBq	7.87 ± 1.12 °C	3	52ph	WE	12.53 %	575 ps	190.69 kcps	0.76 %	13.10 %	0.86 %	142.09 kcps	
83	18.05 MBq	9.26 ± 1.40 °C	1	17ph	NE	12.72 %	270 ps	66.78 kcps	0.70 %	6.15 %	0.34 %	58.05 kcps	
84	18.05 MBq	9.26 ± 1.40 °C	1	17ph	WE	12.75 %	291 ps	131.03 kcps	0.90 %	16.58 %	0.60 %	89.81 kcps	
85	17.52 MBq	9.32 ± 1.45 °C	1	28ph	NE	12.71 %	269 ps	70.73 kcps	0.59 %	6.00 %	0.38 %	61.80 kcps	
86	17.52 MBq	9.32 ± 1.45 °C	1	28ph	WE	12.73 %	288 ps	133.32 kcps	0.74 %	15.97 %	0.64 %	92.96 kcps	
87	13.11 MBq	7.80 ± 1.11 °C	3	28ph	NE	12.44 %	540 ps	112.35 kcps	0.43 %	6.33 %	0.80 %	97.79 kcps	
88	13.11 MBq	7.80 ± 1.11 °C	3	28ph	WE	12.48 %	586 ps	208.40 kcps	0.54 %	15.46 %	1.34 %	147.60 kcps	
89	12.76 MBq	7.79 ± 1.10 °C	3	37ph	NE	12.45 %	539 ps	100.80 kcps	0.42 %	6.19 %	0.74 %	88.02 kcps	
90	12.76 MBq	7.79 ± 1.10 °C	3	37ph	WE	12.47 %	581 ps	179.70 kcps	0.52 %	14.83 %	1.19 %	129.19 kcps	
91	12.42 MBq	7.75 ± 1.09 °C	3	52ph	NE	12.45 %	537 ps	76.50 kcps	0.41 %	5.95 %	0.58 %	67.14 kcps	
92	12.42 MBq	7.75 ± 1.09 °C	3	52ph	WE	12.46 %	574 ps	128.81 kcps	0.50 %	13.35 %	0.90 %	95.89 kcps	
93	11.90 MBq	7.80 ± 1.10 °C	2	17ph	NE	12.44 %	436 ps	104.38 kcps	0.33 %	6.32 %	0.82 %	91.03 kcps	
94	11.90 MBq	7.80 ± 1.10 °C	2	17ph	WE	12.45 %	477 ps	199.32 kcps	0.42 %	16.07 %	1.40 %	139.41 kcps	
95	11.22 MBq	7.81 ± 1.11 °C	2	28ph	NE	12.43 %	435 ps	97.47 kcps	0.31 %	6.25 %	0.81 %	85.17 kcps	
96	11.22 MBq	7.81 ± 1.11 °C	2	28ph	WE	12.45 %	473 ps	180.91 kcps	0.39 %	15.33 %	1.36 %	128.83 kcps	
97	10.71 MBq	8.71 ± 1.28 °C	1	17ph	NE	12.57 %	268 ps	44.42 kcps	0.40 %	6.12 %	0.39 %	38.86 kcps	
98	10.71 MBq	8.71 ± 1.28 °C	1	17ph	WE	12.56 %	289 ps	86.84 kcps	0.53 %	17.11 %	0.67 %	59.15 kcps	

continued on next page

Table S3 – continued from previous page

meas.	activity	system	T_{op}	trig	val	EW	$\Delta E/E$	CRT	prompts	randoms	scatter	sens	NECR
99	10.48 MBq	8.91 ± 1.35 °C	1	28ph	NE	12.55 %	268 ps	46.37 kcps	0.35 %	6.19 %	0.41 %	40.54 kcps	
100	10.48 MBq	8.91 ± 1.35 °C	1	28ph	WE	12.56 %	287 ps	86.98 kcps	0.44 %	15.58 %	0.70 %	61.52 kcps	
101	9.17 MBq	7.83 ± 1.12 °C	3	28ph	NE	12.41 %	540 ps	80.93 kcps	0.30 %	6.18 %	0.83 %	70.84 kcps	
102	9.17 MBq	7.83 ± 1.12 °C	3	28ph	WE	12.42 %	586 ps	149.43 kcps	0.39 %	15.58 %	1.37 %	105.80 kcps	
103	8.82 MBq	7.75 ± 1.11 °C	3	37ph	NE	12.40 %	539 ps	71.63 kcps	0.29 %	6.08 %	0.76 %	62.84 kcps	
104	8.82 MBq	7.75 ± 1.11 °C	3	37ph	WE	12.42 %	581 ps	127.11 kcps	0.37 %	14.75 %	1.23 %	91.80 kcps	
105	8.59 MBq	7.70 ± 1.10 °C	3	52ph	NE	12.39 %	537 ps	54.36 kcps	0.29 %	5.87 %	0.59 %	47.91 kcps	
106	8.59 MBq	7.70 ± 1.10 °C	3	52ph	WE	12.40 %	574 ps	91.15 kcps	0.36 %	14.05 %	0.91 %	66.93 kcps	
107	8.32 MBq	7.74 ± 1.10 °C	2	17ph	NE	12.39 %	435 ps	74.71 kcps	0.23 %	6.20 %	0.84 %	65.44 kcps	
108	8.32 MBq	7.74 ± 1.10 °C	2	17ph	WE	12.41 %	476 ps	142.21 kcps	0.30 %	16.31 %	1.43 %	99.09 kcps	
109	7.87 MBq	7.74 ± 1.10 °C	2	28ph	NE	12.35 %	435 ps	70.10 kcps	0.22 %	6.28 %	0.83 %	61.31 kcps	
110	7.87 MBq	7.74 ± 1.10 °C	2	28ph	WE	12.37 %	473 ps	129.66 kcps	0.28 %	15.57 %	1.39 %	91.99 kcps	
111	6.53 MBq	9.86 ± 1.39 °C	1	17ph	NE	12.61 %	267 ps	26.13 kcps	0.27 %	6.02 %	0.37 %	22.96 kcps	
112	6.53 MBq	9.86 ± 1.39 °C	1	17ph	WE	12.63 %	289 ps	50.49 kcps	0.35 %	16.94 %	0.64 %	34.63 kcps	
113	6.38 MBq	9.39 ± 1.47 °C	1	28ph	NE	12.58 %	268 ps	28.56 kcps	0.22 %	5.68 %	0.42 %	25.30 kcps	
114	6.38 MBq	9.39 ± 1.47 °C	1	28ph	WE	12.60 %	286 ps	53.13 kcps	0.29 %	15.54 %	0.70 %	37.72 kcps	
115	6.17 MBq	8.11 ± 1.26 °C	3	28ph	NE	12.39 %	540 ps	56.04 kcps	0.21 %	6.05 %	0.85 %	49.27 kcps	
116	6.17 MBq	8.11 ± 1.26 °C	3	28ph	WE	12.40 %	585 ps	102.65 kcps	0.27 %	15.61 %	1.40 %	72.78 kcps	
117	6.03 MBq	7.90 ± 1.18 °C	3	37ph	NE	12.36 %	539 ps	50.01 kcps	0.20 %	5.93 %	0.78 %	44.09 kcps	
118	6.03 MBq	7.90 ± 1.18 °C	3	37ph	WE	12.38 %	580 ps	88.34 kcps	0.26 %	15.80 %	1.23 %	62.34 kcps	
119	5.86 MBq	7.79 ± 1.14 °C	3	52ph	NE	12.36 %	536 ps	37.75 kcps	0.20 %	5.83 %	0.61 %	33.35 kcps	
120	5.86 MBq	7.79 ± 1.14 °C	3	52ph	WE	12.38 %	572 ps	62.93 kcps	0.25 %	13.10 %	0.93 %	47.31 kcps	
121	5.63 MBq	7.77 ± 1.11 °C	2	17ph	NE	12.37 %	436 ps	52.15 kcps	0.16 %	6.25 %	0.87 %	45.70 kcps	
122	5.63 MBq	7.77 ± 1.11 °C	2	17ph	WE	12.38 %	476 ps	98.84 kcps	0.21 %	15.91 %	1.47 %	69.64 kcps	
123	5.49 MBq	7.74 ± 1.10 °C	2	28ph	NE	12.34 %	435 ps	49.72 kcps	0.16 %	6.27 %	0.85 %	43.55 kcps	
124	5.49 MBq	7.74 ± 1.10 °C	2	28ph	WE	12.35 %	473 ps	91.81 kcps	0.20 %	15.33 %	1.41 %	65.59 kcps	
125	4.81 MBq	9.07 ± 1.41 °C	1	17ph	NE	12.52 %	268 ps	20.71 kcps	0.19 %	5.91 %	0.40 %	18.27 kcps	

continued on next page

Table S3 – continued from previous page

meas.	activity	system	T_{op}	trig	val	EW	$\Delta E/E$	CRT	prompts	randoms	scatter	sens	NECR
126	4.81 MBq	9.07 ± 1.41 °C	1	17ph	WE	12.53 %	288 ps	40.02 kcps	0.26 %	16.44 %	0.69 %	27.82 kcps	
127	4.65 MBq	9.11 ± 1.44 °C	1	28ph	NE	12.52 %	268 ps	21.56 kcps	0.16 %	5.84 %	0.44 %	19.06 kcps	
128	4.65 MBq	9.11 ± 1.44 °C	1	28ph	WE	12.52 %	286 ps	40.07 kcps	0.22 %	15.76 %	0.72 %	28.33 kcps	
129	3.63 MBq	7.22 ± 1.00 °C	3	28ph	NE	12.37 %	539 ps	33.13 kcps	0.13 %	6.23 %	0.85 %	29.06 kcps	
130	3.63 MBq	7.22 ± 1.00 °C	3	28ph	WE	12.39 %	584 ps	61.73 kcps	0.17 %	15.34 %	1.44 %	44.12 kcps	
131	3.55 MBq	7.46 ± 1.03 °C	3	37ph	NE	12.39 %	538 ps	29.71 kcps	0.13 %	6.09 %	0.79 %	26.14 kcps	
132	3.55 MBq	7.46 ± 1.03 °C	3	37ph	WE	12.40 %	580 ps	53.02 kcps	0.17 %	14.93 %	1.27 %	38.26 kcps	
133	3.34 MBq	7.65 ± 1.08 °C	3	52ph	NE	12.39 %	536 ps	21.78 kcps	0.12 %	5.95 %	0.61 %	19.23 kcps	
134	3.34 MBq	7.65 ± 1.08 °C	3	52ph	WE	12.41 %	573 ps	36.51 kcps	0.16 %	14.28 %	0.94 %	26.75 kcps	
135	3.21 MBq	7.68 ± 1.09 °C	2	17ph	NE	12.40 %	435 ps	29.89 kcps	0.10 %	6.10 %	0.87 %	26.31 kcps	
136	3.21 MBq	7.68 ± 1.09 °C	2	17ph	WE	12.41 %	477 ps	56.77 kcps	0.13 %	15.81 %	1.49 %	40.14 kcps	
137	3.03 MBq	7.67 ± 1.09 °C	2	28ph	NE	12.40 %	433 ps	27.99 kcps	0.09 %	6.10 %	0.87 %	24.63 kcps	
138	3.03 MBq	7.67 ± 1.09 °C	2	28ph	WE	12.41 %	473 ps	51.70 kcps	0.13 %	15.48 %	1.44 %	36.85 kcps	
139	2.78 MBq	9.05 ± 1.43 °C	1	17ph	NE	12.56 %	267 ps	12.28 kcps	0.12 %	6.13 %	0.41 %	10.80 kcps	
140	2.78 MBq	9.05 ± 1.43 °C	1	17ph	WE	12.57 %	288 ps	23.70 kcps	0.17 %	16.76 %	0.71 %	16.38 kcps	
141	2.63 MBq	9.13 ± 1.47 °C	1	28ph	NE	12.54 %	267 ps	12.36 kcps	0.10 %	5.68 %	0.44 %	10.98 kcps	
142	2.63 MBq	9.13 ± 1.47 °C	1	28ph	WE	12.55 %	286 ps	22.98 kcps	0.14 %	15.43 %	0.74 %	16.40 kcps	
143	2.43 MBq	7.92 ± 1.20 °C	3	28ph	NE	12.40 %	539 ps	22.59 kcps	0.09 %	6.03 %	0.87 %	19.91 kcps	
144	2.43 MBq	7.92 ± 1.20 °C	3	28ph	WE	12.42 %	587 ps	41.50 kcps	0.13 %	15.71 %	1.44 %	29.42 kcps	
145	2.35 MBq	7.74 ± 1.14 °C	3	37ph	NE	12.39 %	538 ps	19.94 kcps	0.09 %	6.02 %	0.80 %	17.58 kcps	
146	2.35 MBq	7.74 ± 1.14 °C	3	37ph	WE	12.41 %	581 ps	35.25 kcps	0.12 %	14.58 %	1.28 %	25.66 kcps	
147	2.23 MBq	7.68 ± 1.11 °C	3	52ph	NE	12.39 %	536 ps	14.67 kcps	0.09 %	5.95 %	0.62 %	12.95 kcps	
148	2.23 MBq	7.68 ± 1.11 °C	3	52ph	WE	12.42 %	574 ps	24.53 kcps	0.12 %	13.48 %	0.95 %	18.33 kcps	
149	2.15 MBq	7.66 ± 1.10 °C	2	17ph	NE	12.38 %	435 ps	20.51 kcps	0.07 %	6.06 %	0.90 %	18.07 kcps	
150	2.15 MBq	7.66 ± 1.10 °C	2	17ph	WE	12.40 %	477 ps	38.92 kcps	0.10 %	16.04 %	1.52 %	27.39 kcps	
151	2.08 MBq	7.67 ± 1.10 °C	2	28ph	NE	12.37 %	434 ps	19.30 kcps	0.07 %	6.18 %	0.87 %	16.96 kcps	
152	2.08 MBq	7.67 ± 1.10 °C	2	28ph	WE	12.39 %	474 ps	35.63 kcps	0.10 %	15.34 %	1.45 %	25.49 kcps	

continued on next page

Table S3 – continued from previous page

meas.	activity	system	T_{op}	trig	val	EW	$\Delta E/E$	CRT	prompts	randoms	scatter	sens	NECR
153	1.85 MBq	9.12 ± 1.46 °C	1	17ph	NE	12.53 %	266 ps	8.20 kcps	0.08 %	5.78 %	0.42 %	7.27 kcps	
154	1.85 MBq	9.12 ± 1.46 °C	1	17ph	WE	12.56 %	288 ps	15.84 kcps	0.13 %	16.79 %	0.71 %	10.94 kcps	
155	1.59 MBq	9.12 ± 1.48 °C	1	28ph	NE	12.49 %	266 ps	7.55 kcps	0.07 %	5.79 %	0.45 %	6.69 kcps	
156	1.59 MBq	9.12 ± 1.48 °C	1	28ph	WE	12.51 %	285 ps	14.02 kcps	0.10 %	15.92 %	0.74 %	9.89 kcps	
157	1.50 MBq	7.83 ± 1.19 °C	3	28ph	NE	12.38 %	539 ps	13.95 kcps	0.06 %	6.05 %	0.87 %	12.30 kcps	
158	1.50 MBq	7.83 ± 1.19 °C	3	28ph	WE	12.41 %	589 ps	25.72 kcps	0.10 %	15.40 %	1.45 %	18.38 kcps	
159	1.41 MBq	7.70 ± 1.11 °C	3	37ph	NE	12.36 %	537 ps	12.03 kcps	0.06 %	5.93 %	0.80 %	10.63 kcps	
160	1.41 MBq	7.70 ± 1.11 °C	3	37ph	WE	12.41 %	582 ps	21.31 kcps	0.09 %	14.72 %	1.28 %	15.47 kcps	
161	1.36 MBq	7.65 ± 1.10 °C	3	52ph	NE	12.37 %	537 ps	8.91 kcps	0.06 %	5.84 %	0.62 %	7.89 kcps	
162	1.36 MBq	7.65 ± 1.10 °C	3	52ph	WE	12.38 %	577 ps	14.92 kcps	0.09 %	13.77 %	0.95 %	11.07 kcps	
163	1.03 MBq	7.67 ± 1.10 °C	2	17ph	NE	12.37 %	434 ps	9.84 kcps	0.04 %	6.04 %	0.90 %	8.68 kcps	
164	1.03 MBq	7.67 ± 1.10 °C	2	17ph	WE	12.39 %	479 ps	18.73 kcps	0.07 %	16.12 %	1.52 %	13.16 kcps	
165	0.99 MBq	7.66 ± 1.10 °C	3	28ph	NE	12.36 %	434 ps	9.28 kcps	0.05 %	6.15 %	0.88 %	8.16 kcps	
166	0.99 MBq	7.66 ± 1.10 °C	3	28ph	WE	12.40 %	475 ps	17.31 kcps	0.08 %	15.91 %	1.47 %	12.23 kcps	
167	0.92 MBq	8.86 ± 1.37 °C	1	17ph	NE	12.52 %	266 ps	4.18 kcps	0.05 %	6.02 %	0.43 %	3.69 kcps	
168	0.92 MBq	8.86 ± 1.37 °C	1	17ph	WE	12.53 %	287 ps	8.09 kcps	0.09 %	16.32 %	0.73 %	5.65 kcps	
169	0.88 MBq	9.00 ± 1.44 °C	1	28ph	NE	12.53 %	267 ps	4.23 kcps	0.04 %	6.00 %	0.45 %	3.73 kcps	
170	0.88 MBq	9.00 ± 1.44 °C	1	28ph	WE	12.54 %	285 ps	7.86 kcps	0.08 %	15.86 %	0.75 %	5.56 kcps	
171	0.80 MBq	7.79 ± 1.15 °C	3	28ph	NE	12.36 %	539 ps	7.46 kcps	0.04 %	6.10 %	0.88 %	6.57 kcps	
172	0.80 MBq	7.79 ± 1.15 °C	3	28ph	WE	12.40 %	592 ps	13.77 kcps	0.07 %	15.72 %	1.45 %	9.77 kcps	
173	0.75 MBq	7.68 ± 1.11 °C	3	37ph	NE	12.34 %	537 ps	6.44 kcps	0.04 %	5.98 %	0.80 %	5.69 kcps	
174	0.75 MBq	7.68 ± 1.11 °C	3	37ph	WE	12.43 %	586 ps	11.45 kcps	0.07 %	16.19 %	1.27 %	8.03 kcps	
175	0.72 MBq	7.64 ± 1.09 °C	3	52ph	NE	12.37 %	536 ps	4.74 kcps	0.04 %	5.90 %	0.62 %	4.19 kcps	
176	0.72 MBq	7.64 ± 1.09 °C	3	52ph	WE	12.42 %	579 ps	7.95 kcps	0.07 %	15.62 %	0.93 %	5.65 kcps	
177	0.68 MBq	7.66 ± 1.10 °C	2	17ph	NE	12.35 %	433 ps	6.50 kcps	0.03 %	6.66 %	0.89 %	5.66 kcps	
178	0.68 MBq	7.66 ± 1.10 °C	2	17ph	WE	12.39 %	480 ps	12.38 kcps	0.06 %	16.48 %	1.53 %	8.63 kcps	
179	0.64 MBq	7.66 ± 1.09 °C	2	28ph	NE	12.34 %	434 ps	6.02 kcps	0.03 %	6.21 %	0.87 %	5.29 kcps	

continued on next page

Table S3 – continued from previous page

meas.	activity	system	T_{op}	trig	val	EW	$\Delta E/E$	CRT	prompts	randoms	scatter	sens	NECR
180	0.64 MBq	7.66 ± 1.09 °C	2	28ph	WE	12.42 %	479 ps	11.17 kcps	0.06 %	15.69 %	1.46 %	7.93 kcps	
181	0.61 MBq	7.58 ± 1.08 °C	3	28ph	NE	12.36 %	540 ps	5.70 kcps	0.04 %	6.24 %	0.87 %	5.01 kcps	
182	0.61 MBq	7.58 ± 1.08 °C	3	28ph	WE	12.41 %	597 ps	10.60 kcps	0.07 %	16.18 %	1.46 %	7.44 kcps	
183	0.58 MBq	7.63 ± 1.08 °C	3	37ph	NE	12.33 %	536 ps	4.95 kcps	0.04 %	5.94 %	0.80 %	4.38 kcps	
184	0.58 MBq	7.63 ± 1.08 °C	3	37ph	WE	12.39 %	588 ps	8.85 kcps	0.07 %	15.17 %	1.29 %	6.36 kcps	
185	0.55 MBq	7.63 ± 1.09 °C	3	52ph	NE	12.37 %	535 ps	3.61 kcps	0.04 %	5.77 %	0.62 %	3.21 kcps	
186	0.55 MBq	7.63 ± 1.09 °C	3	52ph	WE	12.43 %	578 ps	6.08 kcps	0.07 %	14.01 %	0.95 %	4.49 kcps	